Applied Thermal Engineering 310 (2026) 134017



Contents lists available at ScienceDirect

Applied Thermal Engineering

journal homepage: www.elsevier.com/locate/apthermeng



Research Paper

Multi-objective optimisation of start-up scheduling for solar-only Micro gas turbine systems

Shahrbanoo Shamekhi [a], Vahid Hosseini [b], Jafar Al-Zaili [a,*], Tehmina Abmreen [b], Abdulnaser Sayma [c]

[a] School of Science & Technology, City St George's, University of London, London EC1V 0HB, UK
[b] School of Physics, Engineering and Computer Science, University of Hertfordshire, Hatfield AL10 9AB, UK
[c] College of Engineering, Design and Physical Sciences, Brunel University of London, Uxbridge UB8 3PH, UK

ARTICLE INFO

Keywords:
Solar MGT
Start-up
Transient
Multi-objective optimisation
Annual performance

ABSTRACT

Solar-only concentrated solar power micro gas turbine (CSP-MGT) systems face unique start-up challenges arising from coupled electro-thermo-mechanical interactions, including compressor surge risk, receiver thermal inertia, and electrical drive constraints, without the benefit of fuel-based regulation. This study presents a multi-objective optimisation framework for start-up scheduling of a 6 kWe parabolic dish CSP-MGT system, based on a validated transient electro-thermo-mechanical model verified against experimental data from the OMSoP project. A three-stage speed schedule is proposed and optimised using NSGA-II across direct normal irradiance (DNI) levels from 300 to 900 W/m^2 and for both warm and cold start-up conditions. A two-stage optimisation procedure first determines the minimum starter capacity for off-grid operation, yielding a recommended design value of 2.5 kWe, then resolves the trade-off between start-up duration and motoring energy consumption. Optimised schedules reduce start-up energy by 30–60% relative to the reference procedure across all DNI levels. Annual simulations using site-specific data from Casaccia, Italy confirm that start-up losses are reduced from 7% to 3% of total annual generation, yielding a 5.3% increase in net electricity output. The framework provides a transferable methodology for start-up optimisation of thermally driven micro power systems.

1. Introduction

As the global energy landscape shifts toward decarbonisation, concentrated solar power (CSP) technologies are gaining renewed attention for their potential to support net-zero carbon goals. In particular, CSP systems offer not only clean energy generation but also the ability to integrate thermal energy storage, enabling dispatchable power that complements variable renewable sources such as photovoltaics and wind [1,2]. Solar energy, specifically solar thermal utilisation, has attracted increased interest in recent years [3], accompanied by rapid expansion in global Concentrated Solar Power (CSP) deployment [4]. Installed capacity reached about 6.7 GW in 2023, and projections indicate that CSP could supply around 11.3% of global electricity demand by 2050, with solar power forming a major share of this contribution [5].

Among CSP technologies, small-scale systems that utilise a micro gas turbine (MGT) as the power conversion engine offer a promising pathway for distributed power generation [6]. These CSP-MGT systems benefit from the thermodynamic efficiency and compact design of micro turbines, while also enabling thermal energy storage integration and high-temperature operation [7]. This combination operates in the Brayton cycle, can work at higher temperatures (more than 700 °C) [4] where valuable advanced outputs can be produced. Importantly, in applications where grid access is unavailable or impractical, such as off-grid systems or geographically remote sites, fully solar-powered MGT configurations, without fuel-based hybridisation, can deliver clean, autonomous electricity generation with minimal operational complexity [8]. However, the intermittent nature of solar input introduces unique challenges, particularly during start-up phases [9–12], which must be carefully managed to ensure reliability, efficiency, and overall system viability.

One of the defining operational characteristics of solar-only CSP-MGT systems is the frequency of start-up and shutdown cycles, driven by the natural intermittency of solar irradiance. Unlike fuelled MGTs or hybrid solar-assisted systems, solar-only configurations cannot modulate input energy on demand, making them particularly sensitive to transient conditions [13–15]. As a result, the start-up phase becomes a

* Corresponding author.
E-mail address: jafar.alzaili@citystgeorges.ac.uk (J. Al-Zaili).

https://doi.org/10.1016/j.applthermaleng.2026.134017
Received 31 July 2026; Received in revised form 27 October 2026; Accepted 8 November 2026
1359-4311/© 2026 The Authors. Published by Elsevier Ltd. This is an open access article under the CC BY license (http://creativecommons.org/licenses/by/4.0/).

Nomenclature

Symbols

A	Area (m^2)
C	Heat capacity (J/K)
c_p	Constant pressure specific heat capacity (J/kg.K)
E	Energy (J)
h	Heat transfer coefficient ($W/m^2.K$)
I	Electric current (Amps)
J	Rotational shaft inertia ($kg.m^2$)
$\dot{m}$	Mass flow rate (kg/s)
N	Rotational shaft speed (rpm)
P	Power (W)
$\dot{Q}$	Heat transfer rate (W)
T	Temperature (K)
t	Time (s)
ε	Emissivity
π	Pressure ratio
σ	Stefan-Boltzmann constant ($W/m^2.K^4$)
τ	Torque (N.m)

Subscripts

A	Alternator
c	compressor
e	Electric
mf,op	modified parameter on operating line
mf,s	modified parameter on surge line
op	Operating
recu	recuperator
recv	receiver
sky	Sky temperature
sol	Solar receiver input heat
sur	Surrounding
s	Surge margins
t	turbine

Abbreviation

CSP	Concentrated solar power
DNI	Direct Normal Irradiation
EGT	Exhaust Gas Temperature
GA	Genetic algorithm
HSA	High Speed Alternator
ISA	International Standard Atmosphere
MGT	Micro Gas Turbine
OMSoP	Optimised Microturbine Solar Power
PMSM	Permanent Magnet Synchronous Machine
SM	Surge Margin
TIT	Turbine Inlet Temperature

critical determinant of system reliability and overall performance. If not managed properly, repeated start-up events can lead to efficiency losses, elevated thermal and mechanical stresses, and accelerated component degradation [16–19].

Several technical challenges emerge during this phase. The first is the risk of compressor surge, which becomes more pronounced at low rotational speeds due to a narrower safe operating region. This issue is further exacerbated in CSP-MGT systems, where large thermal components such as the receiver and recuperator introduce significant downstream pressure losses [20]. Second, the system must contend with thermal inertia, particularly in the solar receiver and recuperator. These components require time to absorb and redistribute heat, and their slow thermal response can cause overheating if airflow and irradiance are not carefully coordinated [18]. Finally, electrical constraints also impose critical limits during start-up. The required torque increases sharply with speed, scaling approximately with the cube of rotational speed, placing high demands on the starter or motor-generator unit. If the available electrical current is insufficient to meet these torque requirements, system control can become unstable or fail entirely. These combined electro-thermo-mechanical interactions make the start-up phase uniquely complex in solar-only MGT systems and warrant a dedicated analysis beyond conventional steady-state performance assessments.

While the transient performance of gas turbine systems has received considerable attention, most studies have focused on either large-scale industrial gas turbines or hybrid solar-assisted micro gas turbines. In the context of large gas turbines, transient analysis has been applied extensively to optimise start-up sequences, reduce fuel consumption, and minimise thermal stress on critical components such as steam turbine rotors [21–24]. These studies have informed advanced control strategies, often using predictive models to balance system flexibility with component longevity.

For micro gas turbines, transient behaviour has also been investigated in solar-hybrid configurations, where a combustion chamber supplements solar input to stabilise thermal power delivery [11,25–28]. For example, Traverso et al. [27] and Chen et al. [28] developed dynamic models of solar-hybrid MGT systems to assess performance under direct normal irradiance (DNI) fluctuations and variable load conditions. Similarly, Yang et al. [13] explored part-load operation of a 10 kWe solar-hybrid MGT with integrated thermal energy storage, identifying heliostat adjustment and gradual load ramping as viable control strategies whereas many studies are limited to quasi steady simulations [20,29,30].

In contrast, solar-only CSP-MGT systems remain relatively underexplored in the transient modelling and control literature. Existing studies have examined specific aspects of solar-only operation, including airflow control under irradiation fluctuations [15] and operation at maximum permissible power [31]. However, these studies have not treated start-up as a constrained scheduling problem in which aerodynamic stability, thermal response, and electrical drive limitations must be satisfied simultaneously. This distinction is important because control strategies developed for fuelled or solar-hybrid MGTs cannot be directly transferred to solar-only systems. In fuelled and hybrid configurations, the combustor provides an actively controllable thermal input that can be used to stabilise the start-up process. In solar-only systems, by contrast, the available thermal input is governed by solar irradiance, receiver absorption, and component thermal inertia. As a result, start-up procedure must coordinate shaft acceleration, dish focusing, receiver heating, and motor-generator operation without relying on fuel-based regulation.

Previous investigations of solar MGT systems have addressed a range of operating and control aspects, as summarised in Table 1. Solar-only studies have primarily considered off-design performance, control under varying solar irradiance, annual performance, and techno-economic optimisation, while transient investigations have focused mainly on system response and control rather than optimisation of the complete start-up trajectory. Start-up has also been considered in solar-hybrid systems; however, these configurations employ auxiliary combustion and differ substantially in system scale and thermal-input control. To the authors' knowledge, no previous study has systematically optimised start-up speed scheduling for solar-only CSP-MGT systems using a validated transient electro-thermo-mechanical model while simultaneously accounting for compressor surge margin, component temperature limits, electrical current constraints, external starter power requirements, and annual energy impact. This represents an important limitation for off-grid and high-cycling applications, where repeated

Table 1
Comparison of previous solar micro gas turbine studies and the scope of the present work.

Study	MGT/ GT size	Solar configuration	Main focus	Start-up studied
Ghavami et al. [31]	5 kWe	Solar-only	Control strategies and annual performance	No
Amelio et al. [15]	100 kWe	Solar-only/ unfired	Dynamic control under DNI/cloud transients	No
Ghavami et al. [2]	5–30 kWe	Solar-only	Off-design and techno-economic optimisation	No
Yang et al. [13]	10 kWe	Solar-assisted with TES	Dynamic operation and real-time control under DNI variations	No
Chen et al. [28]	100 kWe	Solar-hybrid	Dynamic response and control under load/DNI variations	No
Quero et al. [25]	4.6 MWe	Solar-hybrid	Demonstration and operational assessment, including start-up	Yes
Present study	6 kWe	Solar-only	Constrained multi-objective start-up scheduling	Yes

start-up events affect both the technical feasibility and the net energy performance of the system.

This study addresses this gap by integrating a validated transient electro-thermo-mechanical model of a parabolic-dish CSP-MGT system with a multi-objective optimisation framework. The start-up trajectory is parameterised as a multi-stage shaft-speed schedule, including acceleration rates, intermediate speed levels, focusing time, and dwell periods. The optimisation is performed under different DNI levels and for both warm and cold start-up conditions. A two-stage optimisation procedure is adopted. The first stage determines the required external starter capacity by minimising peak motoring power and total motoring energy consumption. The second stage then evaluates the trade-off between start-up duration and motoring energy consumption under the established starter power constraint. All candidate schedules are assessed subject to surge-margin, thermal, mechanical, and electrical constraints.

The optimised schedules are subsequently evaluated within an annual performance framework using site-specific solar data to quantify their impact on start-up energy losses and net electricity generation. This allows the effect of start-up scheduling to be assessed not only at the transient event level, but also in terms of annual system performance and practical off-grid operation.

Building on the previously validated transient CSP-MGT model reported in [32], the present study focuses specifically on start-up scheduling and optimisation. The main contributions are: (i) formulation of the solar-only MGT start-up problem as a constrained multi-objective optimisation that simultaneously accounts for surge margin, component thermal limits and electrical-drive constraints; (ii) development of a two-stage optimisation procedure that first establishes the required starter-power envelope and subsequently determines Pareto-optimal start-up schedules balancing motoring energy and start-up duration over different DNI levels and initial thermal states; and (iii) quantification of the resulting engineering benefits in terms of starter sizing, start-up energy and duration, together with their effect on annual net electricity generation.

2. Methodology

2.1. System configuration

The solar-only concentrated solar power micro gas turbine (CSP-MGT) considered in this study operates on a recuperated Brayton cycle and consists of four primary thermodynamic components: a centrifugal compressor, a solar receiver serving as the heat source, a radial inflow turbine, and a recuperator. A high-speed alternator (HSA) directly coupled to the turbine shaft converts mechanical output to electrical power, while a bi-directional power electronic interface enables motoring during start-up and generation during steady operation. A schematic layout of the system is presented in Fig. 1, while the main design parameters used in this study are summarised in Table 2, respectively.

During operation, ambient air is compressed in the centrifugal compressor and directed to the solar receiver, where concentrated solar radiation is absorbed by the receiver surface and transferred to the working fluid. The high-temperature, high-pressure air expands through the turbine, generating mechanical power to drive both the compressor and the alternator. The turbine exhaust then passes through the recuperator, transferring residual heat to the compressor discharge air before being released to the environment. This heat recovery process improves cycle efficiency by reducing the solar thermal input required to achieve the desired turbine inlet temperature.

The system is designed for off-grid operation, with the electrical starter power supplied by an external battery. In the motoring phase, the alternator operates as a permanent magnet synchronous motor (PMSM), drawing power through the converter to accelerate the shaft to the target rotational speed. Once sufficient thermal power is available from the receiver to achieve self-sustaining operation, the machine transitions to generation mode, supplying electrical power to the connected load or storage. This configuration ensures autonomous operation in remote locations but places strict requirements on start-up power demand, battery capacity, and the thermal–mechanical constraints of key components.

2.2. Transient electro-thermo-mechanical model

The dynamic behaviour of the CSP-MGT system during start-up was simulated using a transient electro-thermo-mechanical model developed in MATLAB/Simulink. The modelling approach, previously detailed and validated in [32] using experimental data from the OMSoP project [19,29], integrates thermodynamic, electrical, mechanical and control subsystems into a coupled simulation environment to capture the interactions governing start-up performance. The overall architecture of the model, showing the coupling between these subsystems, is illustrated in Fig. 2. The developed dynamic model is capable of simulating the key transient responses in real time. It also captures the MGT start-up sequence by accounting for the low-speed performance characteristics of the compressor and turbine. The CSP-MGT model comprises the main system components, including the compressor, turbine, solar receiver, recuperator, and shaft. In addition, an artificial plenum component is introduced to represent mass imbalance effects associated with the relatively large internal volumes of the recuperator and solar receiver.

The performance parameters of each component are determined using a combination of conservation laws and performance maps. The recuperator and receiver are treated as one-dimensional volumes, in

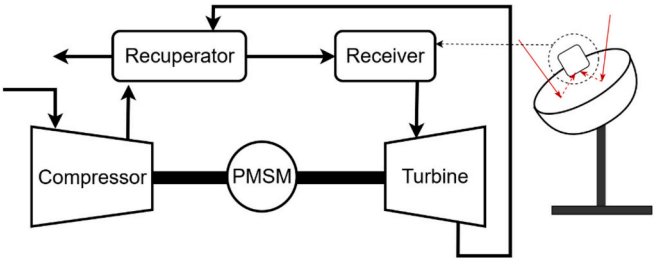


Fig. 1. Schematic of a CSP-MGT system.

Table 2
Design parameters of the 6 kWe CSP-MGT system.

Parameter	Value	Unit
Output power	6	kW_e
Shaft speed	130	krpm
Turbine Inlet Temperature (TIT)	1073	K
Turbine Exhaust Temperature (TET)	923	K
Compressor pressure ratio	3	–
Air mass flow rate	0.088	kg/s
DNI	800	W/m^2

which the energy conservation equations are applied in unsteady form to account for heat soakage. The momentum equation is applied in steady-state form to determine the pressure drop across these two components. The plenum is modelled using a transient continuity equation to account for mass accumulation within the recuperator and receiver. For the compressor and turbine, the operating points are determined from their respective performance maps. Their transient thermal behaviour is represented by adding an additional 0-D lumped volume in series with each component. However, mass accumulation in the compressor and turbine is neglected because their internal volumes are small compared with those of the recuperator and receiver. The thermodynamic properties of air are computed using temperature-dependent correlations reported by [33].

2.2.1. Turbomachinery

The compressor and turbine are each represented using two sequential calculations, as described above. The first calculation uses a quasi-steady-state approach to determine the outlet parameters from the performance maps. The second calculation incorporates a 0-D lumped-volume model to account for heat soakage. The low-speed region of the compressor and turbine maps was generated with the software of GasTurb, using Kurzke's β-line method [34]. Speed lines were interpolated along β-lines toward a zero-speed line for the compressor and a zero-speed point for the turbine and then tuned to measured low-speed operating points so that each generated line lies within the measurement uncertainty of its operating point. The resulting map uncertainty is about ±1.5% in pressure ratio and ±5 – 6.5% in mass flow, rising to about ±19% in mass flow at the lowest compressor speed [32]. This higher uncertainty is limited to the initial low-speed phase of start-up.

That said, the quasi-steady compressor outlet temperature, neglecting thermal interaction between the air and the compressor metal, is calculated as eq. (1).

$$T_{2'} = T_1\left(1+\frac{1}{\eta_c}\left[\pi_c^{\frac{\gamma-1}{\gamma}}-1\right]\right) \tag{1}$$

where $T_{2'}$, T_1,η_c,π_c,γ are the quasi-steady compressor outlet temperature, compressor inlet temperature, isentropic efficiency, compressor pressure ratio and specific heat ratio.

In the second step, the quasi-steady outlet temperature is corrected by accounting for heat exchange between the compressed air and the compressor casing metal, as shown schematically in Fig. 3 as eq. (3).

$$\dot{Q}_{m,c} = h_c A_c\left(T_{a,c}-T_{m,c}\right) = M_c c_c \frac{dT_{m,c}}{dt} \tag{2}$$

$$T_2 = T_{2'} - \frac{\dot{Q}_{m,c}}{\dot{m}_c c_{p,c}} \tag{3}$$

where h_c, $A_c$are the heat transfer coefficient and heat transfer area be-

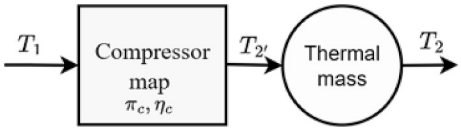


Fig. 3. The serial calculation approach of the compressor.

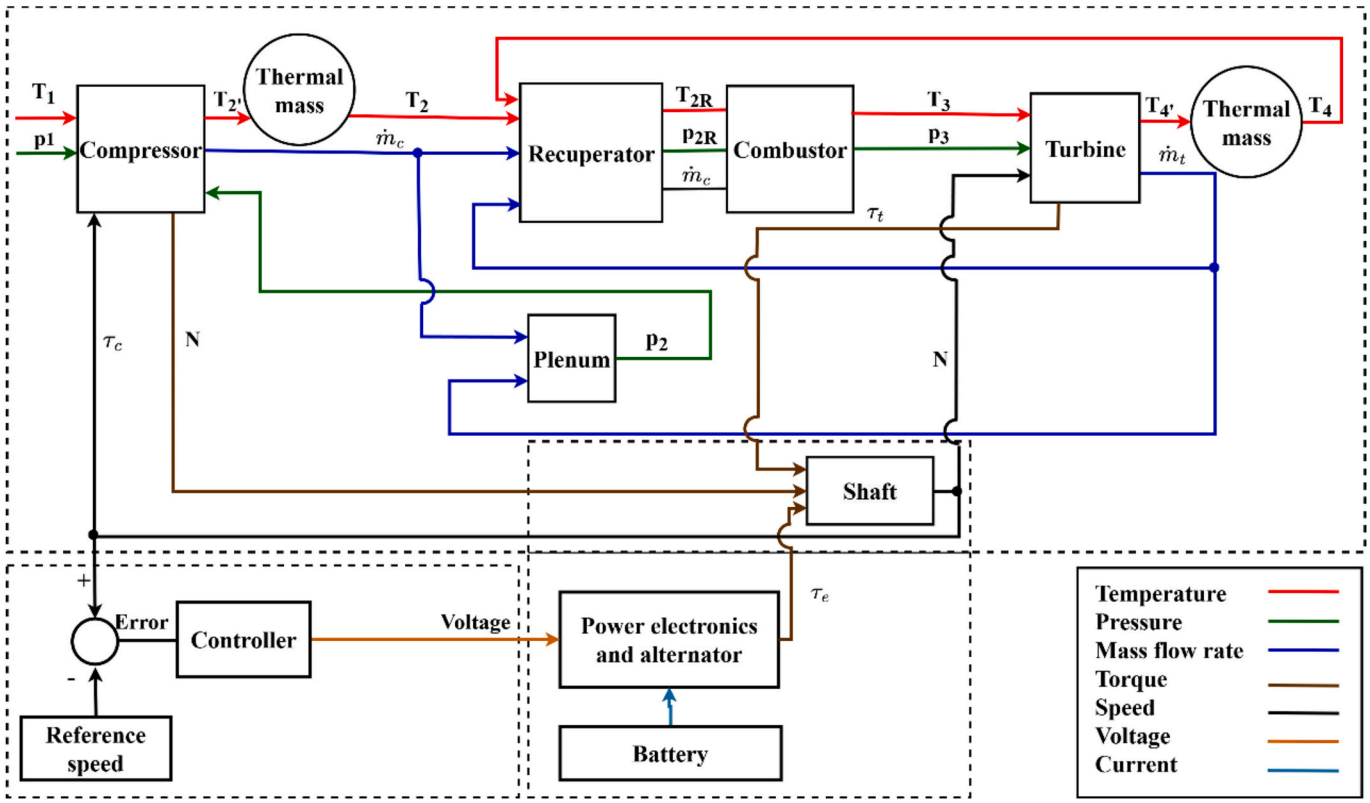


Fig. 2. The layout of the developed electro-thermo-mechanical model in MATLAB/Simulink.

tween compressor air and compressor metal. $T_{a,c}$ and $T_{m,c}$ are the average air temperature of the compressor and mean wall temperature of compressor metal. M_c and c_c are the compressor casing metal mass and heat capacity. $\dot{Q}_{m,c}$, $\dot{m}_c$ and $c_{p,c}$ are heat transfer rate between compressor air and compressor casing metal, compressor air mass flow rate and specific heat capacity. $\dot{Q}_{m,c}$ is positive when heat flows from the air to the casing and negative in the reverse direction.

A similar approach is used to calculate the turbine outlet temperature. The turbine quasi-steady outlet temperature, and the corrected turbine outlet temperature are calculated with eqs. (4) and (5), respectively.

$$T_{4'} = T_3\left(1+\frac{1}{\eta_t}\left[\frac{1}{\pi_t}^{\frac{\gamma-1}{\gamma}}-1\right]\right) \tag{4}$$

where T_4, T_3,η_t,π_t are the turbine quasi-steady outlet temperature, turbine inlet temperature, isentropic efficiency and turbine pressure ratio.

$$T_4 = T_{4'} - \frac{Q_{m,t}}{\dot{m}_t c_{p,t}} \tag{5}$$

where T_4,η_t,π_t are the turbine outlet temperature. $\dot{Q}_{m,t}$ is the heat transfer rate to the turbine casing metal that can be estimated by solving eq. (6).

$$\dot{Q}_{m,t} = h_t A_t\left(T_{a,t} - T_{m,t}\right) = M_t c_t \frac{dT_{m,t}}{dt} \tag{6}$$

where h_t, $A_t$are the heat transfer coefficient and heat transfer area between turbine air flow and turbine casing metal. $T_{a,t}$ and $T_{m,t}$ are the average air temperature in the turbine and mean wall temperature of turbine metal. M_t and c_t are the turbine casing metal mass and heat capacity.

Having the outlet temperatures, the compressor power consumption and turbine generated power are first calculated from the quasi-steady air-side enthalpy changes, before applying the thermal-mass correction, using eqs. (7) and (8).

$$P_{c'} = \dot{m}_c c_{p,c}(T_{2'} - T_1) \tag{7}$$

$$P_{t'} = \dot{m}_t c_{p,t}(T_3 - T_{4'}) \tag{8}$$

where $\dot{m}_c$, $\dot{m}_t$, $c_{p,c}$, $c_{p,t}$, T_1, $T_{2'}$, T_3 and $T_{4'}$ are the compressor mass flow rate, turbine mass flow rate, compressor air heat capacity, turbine air heat capacity, compressor inlet temperature, compressor quasi-steady outlet temperature, turbine inlet temperature and turbine outlet quasi-steady temperature, respectively.

The heat soakage of the turbine calculated $\dot{Q}_{m,t}$, eq. (6), reduces the useful turbine power because part of the gas-side energy is absorbed by the turbine metal during transient operation. Therefore, the corrected turbine power is written as eq. (9).

$$P_t = P_{t'} - Q_{m,t} \tag{9}$$

The compressor power consumption is kept equal to its quasi-steady value, eq. (10).

$$P_c = P_{c'} \tag{10}$$

where P_c, P_t and $Q_{m,t}$ are the corrected compressor power consumption, corrected turbine generated power, and heat transfer rate from the turbine air to the turbine metal, respectively.

2.2.2. Solar receiver

The solar receiver is modelled as an impinging cavity receiver, following the configuration adopted in [35]. In this design, jet impingement is introduced into a conventional cavity receiver to enhance convective heat transfer from the absorber surface to the working fluid. The thermal power delivered to the receiver by the parabolic dish is calculated as eq. (11).

$$\dot{Q}_{sol} = DNI\, A_{eff}\eta_{opt} \tag{11}$$

where DNI, A_{eff} and η_{opt} are the direct normal irradiance, effective solar dish area, and optical efficiency of the parabolic dish, respectively.

Regarding radial non-uniformity, an initial assessment was conducted at the highest heat flux of 57 $kW/m2$, using the thermo-mechanical properties of the receiver material and a wall thickness of 3 mm. The maximum radial temperature gradient obtained was below 5 K. The mean wall temperature was therefore adopted as the constraint representing the overall thermal state of the receiver, and local temperature gradients were not modelled explicitly. For the ith receiver cell, the transient energy balance is written as:

$$\frac{1}{n}M_{rec}c_{rec}\frac{dT_{rec}{}^{i}}{dt} = \frac{1}{n}\dot{Q}_{sol} - \dot{Q}_{abs}{}^{i} - \frac{1}{n}\dot{Q}_{loss} \tag{12}$$

where M_{rec}, c_{rec}, $T_{rec}{}^{i}$, $A_{rec}{}^{i}$, $\dot{Q}_{sol}$, and $\dot{Q}_{loss}$ are the receiver metal mass, receiver heat capacity, wall temperature of the ith cell, total solar heat input to the receiver, and total heat loss from the receiver cavity to the ambient environment, respectively. The receiver heat loss includes both convective and radiative losses from the cavity surface [36].

The absorbed heat by the air in each cell can be calculated as eq. (13):

$$\dot{Q}^{i}_{abs} = h^{i}_{rec}A^{i}_{rec}\left(T^{i}_{m,rec} - \frac{T^{i}_{rec,in}+T^{i}_{rec,out}}{2}\right) \tag{13}$$

where h^{i}_{rec} and A^{i}_{rec} are the local convective heat transfer coefficient and heat transfer area of the ith receiver cell, respectively. $T^{i}_{m,rec}$, $T^{i}_{rec,in}$ and $T^{i}_{rec,out}$ are the receiver absorber wall temperature, the air temperatures at the inlet and outlet of the ith cell. The subscripts abs, rec, in, and outdenote absorbed heat, receiver, inlet, and outlet, respectively.

The local heat transfer coefficient is calculated as a function of the distance from the stagnation point, where the impinging jet strikes the receiver surface. For cells located within the impingement-dominated region, the local Nusselt number is evaluated using the correlation proposed by [37], as given in eq. (14):

$$Nu_x = 0.055 Re_{st}{}^{0.75} Pr^{0.42} e^{-0.025(x/d)^2}, \qquad 0 \le x/d \le 8$$

$$h_x = \frac{Nu_x k_{air}}{d}$$

$$Re_{st} = \frac{4\,\dot{m}}{\mu n_{nozzle}\pi d} \tag{14}$$

where x, d, k_{air}, μ and n_{nozzle} are the distance from the stagnation point, nozzle diameter, air thermal conductivity, air dynamic viscosity, and the number of nozzles on the receiver, respectively. The subscripts of x and st refer to the distance from the stagnation point and stagnation point. For the cells, where $x/d > 8$, the local heat transfer coefficient is calculated using the Dittus–Boelter correlation [38], as the flow is no longer dominated by the direct impingement region.

The pressure drop in the receiver is mainly associated with the jet impingement process and is calculated as eq. (15).

$$\Delta p = \frac{\rho V_{jet}{}^{2}}{2\, C_d{}^{2}} \tag{15}$$

where ρ, V_{jet}, C_d are jet air density, jet velocity and discharge coefficient, respectively.

2.2.3. Recuperator

The recuperator considered in this study is a plate-fin heat exchanger

which operates close to its design performance point [39]. It is modelled using a one-dimensional discretised approach, in which the heat exchanger is divided into n control volumes along the flow direction. Each control volume consists of a recuperator wall element, a hot-side air stream, and a cold-side air stream. This formulation allows the transient thermal response of the recuperator matrix to be captured while maintaining a computationally efficient model. For the ith recuperator element, the transient energy balance of the solid matrix is expressed as:

$$\frac{1}{n}M_{rec}c_{recu}^{i}\frac{dT_{recu}^{i}}{dt}=\dot{Q}_{hot}^{i}-\dot{Q}_{cold}^{i} \tag{16}$$

where M_{rec} c_{recu}^{i}, T_{recu}^{i} are the recuperator metal mass, the heat capacity and temperature of the ith recuperator element, respectively. $\dot{Q}_{hot}^{i}$ is the heat transferred from the hot-side air to the recuperator wall, while $\dot{Q}_{cold}^{i}$ is the heat transferred from the recuperator wall to the cold-side air which their values are calculated as eqs. (17) and (18), respectively.

$$\dot{Q}_{hot}^{i}=\dot{m}_{hot}c_{p,hot}\left(T_{hot}^{i}-T_{hot}^{i-1}\right)=\frac{h_{hot}A_{hot}}{n}\left(\frac{T_{hot}^{i}+T_{hot}^{i-1}}{2}-T_{recu}^{i}\right) \tag{17}$$

$$\dot{Q}_{cold}^{i}=\dot{m}_{cold}c_{p,cold}\left(T_{cold}^{i}-T_{cold}^{i-1}\right)=\frac{h_{cold}A_{cold}}{n}\left(\frac{T_{cold}^{i}+T_{cold}^{i-1}}{2}-T_{recu}^{i}\right) \tag{18}$$

where $\dot{Q}_{hot}^{i}$ and $\dot{Q}_{cold}^{i}$ are the heat transfer rate from the hot side air to the recuperator metal mass and the heat transfer rate from the recuperator metal mass to the cold side air. $\dot{m}_{hot}$, $\dot{m}_{cold}$, $c_{p,hot}$, $c_{p,cold}$, h_{hot}, h_{cold} and A_{hot}, A_{cold} are hot side and code side air mass flow rate, heat capacity, heat transfer coefficient and heat transfer area. T_{hot}^{i}, T_{cold}^{i} and T_{recu}^{i} are the ith discretised element of the recuperator thermal model for hot side air, cold side air and recuperator metal mass.

The heat transfer coefficient for the plate-fin heat exchanger is calculated using the correlation form [40], eq. (19).

$$h=\frac{j\,G\,c_p}{Pr^{2/3}} \tag{19}$$

where j is Colburn factor, c_p is the specific heat capacity, and Pr is the Prandtl number. G is fluid mass velocity based on the minimum free-flow area ($\dot{m}/A$) where A is the cross-section of the fluid. This equation has been shown to be valid for the range of 100 to 3500 [2]. Since the initial speed for all of the solutions is 100 rpm, the accepted Reynolds range is in the range of simulation Reynolds.

The pressure drops on both the hot and cold sides of the recuperator is calculated using eq. (20).

$$\Delta p=\frac{4fLG^2}{2D_h}\frac{1}{\rho_m} \tag{20}$$

where f, L, $D_h$and ρ_m are fanning friction factor, airflow length on one side of the heat exchanger, hydraulic diameter, and the average of inlet and outlet fluid density, respectively. The mean density value (ρ_m) is evaluated from $\frac{1}{\rho_{in}}+\frac{1}{\rho_{out}}=\frac{1}{\rho_m}$ where $\rho_{in}$and ρ_{out} the inlet and outlet air densities of the corresponding flow stream.

2.2.4. Shaft, electrical system, plenum, and control

The shaft is modelled as a 0-D rotating component, where its transient behaviour is governed by the balance between the power generated by the turbine, the power consumed by the compressor, mechanical losses, and the electrical power exchanged with the PMSM. The shaft dynamic equation is written as eq. (21).

$$J(2\pi/60)^2N\frac{dN}{dt}=P_t-P_c-P_{m,loss}-P_e-P_{e,loss} \tag{21}$$

where J, N, P_t, P_c, $P_{m,loss}$, P_e and $P_{e,loss}$ are the shaft rotational inertia, shaft speed, turbine generated power, compressor power consumption, mechanical power loss, electrical power exchanged with the PMSM, and electrical loss, respectively. In this formulation, P_e is taken as positive when electrical power is extracted from the shaft during generation, and negative when electrical power is supplied to the shaft during motoring.

The electrical power is supplied to, or extracted from, the permanent magnet synchronous machine (PMSM) through the bi-directional power electronic converter. During start-up, the PMSM operates in motoring mode and accelerates the shaft by drawing power from the external battery through the converter. Once the system reaches self-sustaining operation, the PMSM transitions to generating mode and delivers electrical power to the load or storage system. The arrangement of the electrical system in motoring mode is shown in Fig. 4.

Mechanical losses are mainly attributed to bearing losses which is calculated using the empirical relation given by [33], as eq. (22).

$$P_{m,loss}=4.87\times10^{-5}\left(D^{3.95}N^{1.75}{\mu_{oil}}^{0.4}\right)+3.19\times10^{-10}\left(ND\dot{m}_{oil}\right) \tag{22}$$

where D, μ_{oil} and $\dot{m}_{oil}$ are pitch circle diameter of the bearing, oil viscosity and oil mass flow rate. The oil mass flow rate is assumed to remain constant with the value of 0.3 kg/min in this study [41].

In this study, the electrical losses are assumed to arise solely from the PMSM, while losses in the bi-directional converter are neglected. Accordingly, the PMSM electrical loss is calculated using eq. (23), following [2]:

$$P_{e,loss}=3R_{HSA}{I_{RMS}}^2+K_{HSA}N \tag{23}$$

where R_{HSA}, I_{RMS}, K_{HSA} and N are the PMSM ohmic resistance, RMS current, power gain coefficient and rotational speed, respectively.

The plenum is introduced to account for volume dynamics associated with the relatively large internal volumes of the recuperator and solar receiver. These volumes cause a delay between changes in compressor discharge flow and the corresponding pressure response upstream of the turbine. The pressure dynamics are represented using the transient continuity Eq. [42] as eq. (24).

$$\frac{dp_2}{dt}=\frac{RT_2}{V_{plenum}}\left(\dot{m}_c-\dot{m}_t\right) \tag{24}$$

where p_2, R, T_2, and V_{plenum} are compressor outlet pressure, gas constant, compressor outlet temperature, and plenum volume, respectively. The plenum volume includes the internal air volume of the recuperator and receiver.

The control system uses a proportional-integral (PI) controller to track the reference shaft-speed profile defined by the start-up schedule. The controller adjusts the PMSM torque within the allowable electrical limits and coordinates the dish focusing command to regulate the thermal input to the receiver.

2.2.5. Validation of the transient electro-thermo-mechanical model

The model has been validated against experimental data obtained from the CSP-MGT prototype tested within the OMSoP project [32]. The main model parameters and material properties used in the simulations are summarised in Table 3, Table 4, and Table 5.

Fig. 5 shows comparisons between simulated and measured transient responses for key thermodynamic and performance parameters, including, Turbine Inlet Temperature (*TIT*), Exhaust Gas Temperature (*EGT*), and the compressor and turbine pressure ratios (π_c and π_t). The

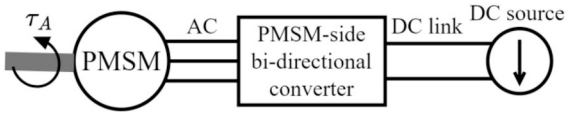


Fig. 4. The schematic of the electrical system components and their arrangement in the motoring mode for off-grid conditions.

results show good agreement in both magnitude and dynamic trends. The Root Mean Square Error (RMSE) values for TIT is 32.87 K, and for EGT are 12.70 K, corresponding to relative errors of 7.71% and 3.87% with respect to the mean experimental values, respectively. The larger deviation in TIT is attributed to the transient overshoot during the acceleration phase, where the simplified thermal model of the receiver and recuperator does not fully resolve the localised heat redistribution. For the pressure ratios, the RMSE values are 0.067 for π_c and 0.075 for π_t, representing relative errors of 5.22% and 5.91%, respectively, and falling within acceptable bounds for a transient model of this complexity. The validation confirms that the model reliably captures the coupled thermal, mechanical, and electrical dynamics of the system, making it suitable for evaluating and optimising start-up schedules under varying solar conditions.

The model assumes International Standard Atmosphere (ISA) conditions at sea level for ambient inputs, and off-grid operation where all motoring power is provided by the external battery. These assumptions focus the analysis on the internal system dynamics rather than on environmental variability. The resulting integrated model provides a high-fidelity yet computationally efficient methodology for evaluating alternative start-up schedules under varying solar irradiance conditions. It forms the basis of the optimisation framework of this paper.

2.3. Optimisation framework

2.3.1. Start-up scenarios and initial conditions

The start-up process is first classified into two types, warm and cold, based on the initial thermal state of the system. Unlike fuelled micro gas turbines, where start-up classification is often linked to the duration of shutdown, the solar-only CSP-MGT requires a more direct thermal metric. In this work, the start-up thermal state is classified using the mean recuperator wall temperature, which provides a practical indicator of the residual thermal energy stored in the system and correlates with the thermal condition of the turbine flow path.

A cold start-up corresponds to components at ambient temperature, typical for early morning operation. A warm start-up is defined when the recuperator wall temperature and other component temperatures remain elevated from recent operation, as determined from OMSoP experimental measurements [18]. The initial temperature values for the receiver, recuperator, turbine casing, and compressor casing used in the simulations are listed in Table 6. These conditions are applied at the beginning of the transient simulation and influence the heating rates, surge margin, and electrical load requirements during the start-up.

In solar-only CSP-MGT systems, the start-up phase must be managed to ensure both operational reliability and efficiency under varying solar input conditions. Since thermal power input cannot be actively regulated by fuel flow, the start-up trajectory is defined in terms of shaft-speed evolution. In this study, the schedule to be optimised is expressed as a sequence of discrete speed stages, each characterised by a target rotational speed, a rate of acceleration or deceleration, and an optional dwell time. This sequential format offers greater flexibility in meeting system constraints compared to a single continuous ramp profile, allowing the schedule to be adapted to the thermal and electrical limitations at different stages of start-up.

Table 3
Thermo-mechanical component parameters used in the transient model.

Parameter	Value	Unit
Compressor metal mass (M_c)	1.38	[kg]
Turbine metal mass (M_t)	2.15	[kg]
Recuperator metal mass (M_{recu})	50	[kg]
Receiver metal mass (M_{recv})	20	[kg]
Nozzle diameter (d)	0.01	m
Number of nozzles (n_{nozzle})	12	–

Table 4
Solar dish parameters.

Parameter	Value	Unit
Dish area (A_{dish})	88	m^2
Optical efficiency (η_{opt})	0.409	–

Table 5
Electrical machine and shaft parameters.

Component	Parameter	Unit	Value
PMSM	K_{HSA}	W/krpm	2.28
Shaft	Inertia	$Kg.m^2$	1.1×10^{-4}

2.3.2. Start-up schedule parameterisation and decision variables

The general form of the start-up schedule used in this work is shown in Fig. 6, where the shaft speed increases from rest to the rated speed for the given DNI through a series of intermediate steps. A stepped start-up schedule was adopted based on practical operational experience gained during the OMSoP project, where repeated system operation highlighted the importance of gradual thermal loading and robust, low-complexity control during start-up. Three steps were selected as a practical compromise, providing sufficient resolution to manage initial focusing, thermal stabilisation, and approach to nominal operation without introducing unnecessary control or scheduling complexity.

- Stage 1 (dwell at N_1): The system must reach a minimum speed before focusing the dish, to avoid receiver overheating from stagnant airflow. The dwell then allows the receiver and recuperator to absorb and redistribute heat before further acceleration, which would otherwise push surge margin below the safe threshold.
- Stage 2 (dwell at N_2): A second thermal stabilisation point is needed because the recuperator, due to its large thermal mass, continues to heat up after the receiver, and the turbine inlet temperature is still rising. Accelerating directly to rated speed from N_1 would risk exceeding the current limit or turbine temperature constraint.
- Stage 3 (ramp to N_3): Final acceleration to the DNI-specific rated speed once thermal equilibrium is sufficiently approached.

The physical necessity of three stages is further confirmed by the optimisation results presented in Section 3, where the algorithm never produced a feasible solution with fewer than three stages. The defining parameters are summarised in Table 7. The first stage begins with acceleration to the "focus speed" N_1, at which point the solar dish is directed toward the receiver to begin thermal input. This is followed by a dwell period Δt_1 to allow the receiver and recuperator to absorb and redistribute heat. The shaft then accelerates to a second constant speed N_2 at rate RN_2, with a second dwell period Δt_2, before the final acceleration to the rated speed N_3 at rate RN_3. The rated speed N_3 corresponds to the maximum permissible power (adapted from Ghavami et al. [2,31]) for the prevailing DNI and is held until the onset of power generation. It should be mentioned that the initial speed for all of the simulations has been chosen to be 100 rpm.

In the optimisation framework, the decision variables are the schedule parameters that define the intermediate speeds, acceleration rates, focusing time, and dwell periods. The decision vector is therefore defined as eq. (25):

$$\mathbf{x} = \left[N_1, RN_1, t_f, \Delta t_1, N_2, RN_2, \Delta t_2, RN_3\right] \tag{25}$$

The final rated speed (N_3) is not treated as an independent decision variable. Instead, it is fixed for each DNI level based on the maximum permissible power condition of the system.

2.3.3. Objective functions

The objective of the optimisation is to determine start-up speed

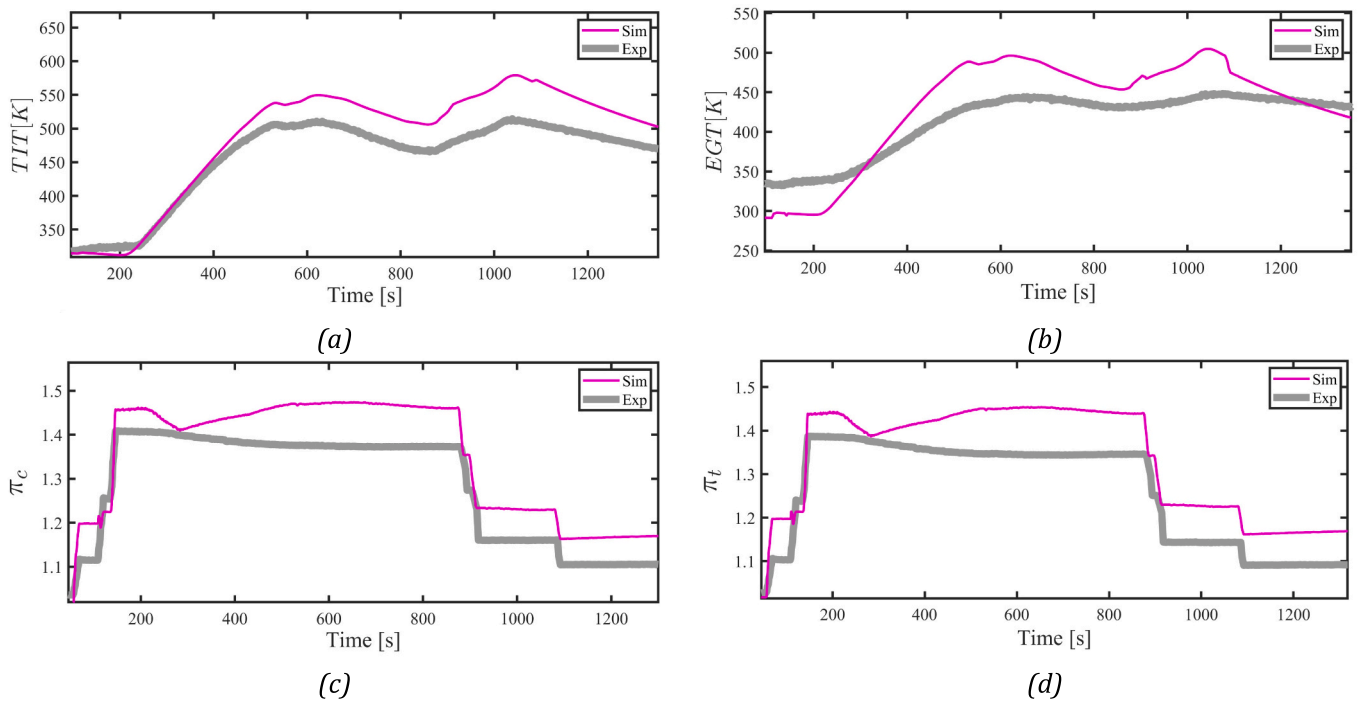


Fig. 5. Validation of the transient electro-thermo-mechanical model against experimental data from the CSP-MGT prototype tested in the OMSoP project [41]. (a) Turbine Inlet Temperature (TIT), (b) Exhaust gas temperature (EGT). (c) Compressor pressure ratio (π_c), and (d) turbine pressure ratio (π_t).

Table 6
Initial conditions for the four temperatures of the state variables belonging to the two types of start-ups.

Parameter	Warm start-up [K]	Cold start-up [K]
Receiver mean wall temperature	405	288
Recuperator mean wall temperature	393	288
Turbine mean casing temperature	397	288
Compressor mean casing temperature	308	288

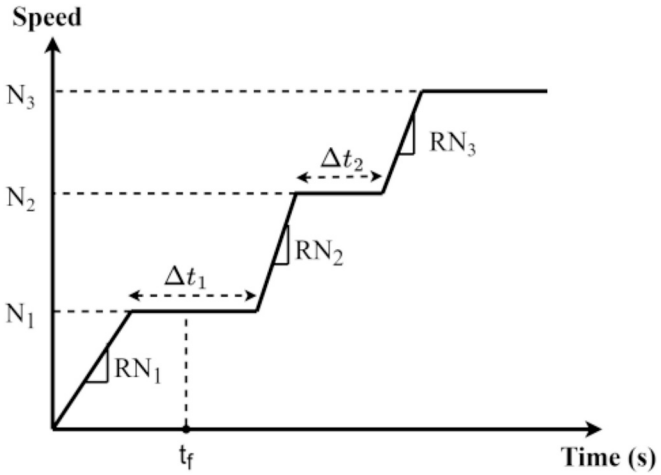


Fig. 6. The defining parameters of the CSP-MGT start-up speed schedule.

schedules that minimise the required motoring power, total energy consumption, and start-up duration (which are introduced in eq. (26) to (28)) while satisfying all operational constraints. The optimisation process integrates the transient electro-thermo-mechanical model with a multi-objective search algorithm, allowing simultaneous evaluation of performance, reliability, and operational limits.

Table 7
Definition of each defining parameter of the CSP-MGT start-up speed schedule.

Parameter	Definition	Role
N_1 [krpm]	First resting speed (Focus speed)	Decision variable
RN_1 [krpm/s]	First speed change rate	Decision variable
t_f [s]	Focus time	Decision variable
Δt_1 [s]	First resting time period	Decision variable
N_2 [krpm]	Second resting speed	Decision variable
RN_2 [krpm/s]	Second speed change rate	Decision variable
Δt_2 [s]	Second resting time period	Decision variable
N_3 [krpm]	Third resting speed	Fixed for each DNI
RN_3 [krpm/s]	Third speed change rate	Decision variable

$$P_{max} = max(|P_e(t)|) \tag{26}$$

$$E_{start} = \int_0^{t_{gen}} -P_e(t)dt \tag{27}$$

$$t_{start} = t_{gen} - t_0 \tag{28}$$

where $P_e(t)$, t_{gen}, and t_0 are the electrical power drawn from the battery via the converter during start-up, time to reach the onset of power generation, and time at which motoring begins, respectively.

2.3.4. Operational constraints

Decision variables, Eq. (25), are limited by a few operation constraints which are enforced in the optimisation framework:

- Thermal limits: maximum temperatures for the receiver, recuperator, and turbine must not exceed design values.
- Compressor surge margin: must remain above 15% [33] for all operating points.
- Electrical limits: PMSM current must not exceed the maximum allowable value i_{max} during motoring mode.
- Mechanical limits: shaft acceleration rates must remain within the bounds defined for each stage.

Thermal constraints on the receiver, recuperator, turbine, and compressor are implemented directly in the model, along with surge-margin calculations for the compressor using eq. (29) as outlined in [43]:

$$SM = \left(\frac{\pi_s}{\pi_{op}} \frac{\dot{m}_{mf,op}}{\dot{m}_{mf,s}} - 1 \right) \times 100 \quad (29)$$

where *SM, ṁ, π* are the compressor's surge margin, mass flow, pressure ratio, and the subscripts *s*, *op*, *mf,s* and *mf,op* refer to the parameter on surge line, parameter on operating line, modified parameter on the surge line and modified parameter on operating line, respectively.

The details of the constraint values are listed in Table 8.

2.3.5. Optimisation procedure

The optimisation procedure is implemented in two stages to reflect the design logic of the system. In the first stage, the optimisation is carried out using maximum motoring power and total motoring energy consumption as the objectives. In this stage, the aim is to determine the required electrical capacity of the system during start-up, which is directly related to starter and battery sizing. For this reason, the optimisation considers the maximum power requirement and the total energy consumption as the two objective functions. These parameters define the power rating and energy capacity of the starter and battery, respectively. The start-up duration is not included as an objective in this stage, as it does not directly influence the sizing of the electrical system. Furthermore, the effect of start-up duration is inherently reflected in the total energy consumption, which represents the integral of power over time. Including time as an additional objective would therefore introduce redundancy and unnecessarily increase the complexity of the multi-objective optimisation without providing additional design insight. This step establishes the peak starter power requirement across different DNI levels, which directly informs the sizing of the battery and power electronics for off-grid operation.

Once the starter capacity was fixed, the second stage of the optimisation focused on the trade-off between start-up duration and motoring energy consumption, generating Pareto-optimal schedules that satisfy the previously determined starter power limit. This two-step procedure ensures that both hardware sizing and operational efficiency are systematically addressed.

A multi-objective genetic algorithm (GA) based on the NSGA-II framework is employed due to its robustness in handling nonlinear, multi-constraint problems and its suitability for discrete decision variables [44] The GA operates on a population of candidate schedules, evolving them through selection, crossover, and mutation operators. At each generation, the transient model evaluates the candidate schedule, computes objective values, and checks constraint compliance. Any candidate solution that violates one or more operational constraints during the transient simulation is rejected and excluded from the population, ensuring that all solutions on the Pareto front are physically feasible [44].

In the present study, the GA parameters were selected to ensure a well-converged and well-distributed Pareto front at a reasonable computational cost. The crossover fraction was set to 0.8 with a scattered crossover function, mutation was handled by the adaptive feasible operator, and the Pareto fraction was set to 0.35, in line with established NSGA-II practice for constrained problems [44]. The optimisation was considered converged when the change in the spread of the Pareto-front solutions fell below a tolerance of 1×10^{-4}; the adequacy of this criterion was verified by tracking the hypervolume (HV) of the Pareto front across generations, as discussed in Section 3.2. The HV measures how close a Pareto front lies to the ideal point and how wide a range of trade-offs it covers. The population size was selected through a sensitivity analysis of sizes between 30 and 300. Each resulting Pareto front was evaluated using the HV and the inverted generational distance (IGD), defined as the average distance from the best known Pareto front to the nearest solution on the evaluated front. Front quality improved markedly up to approximately 125 individuals and showed no significant trend beyond this point; a population of 300 was therefore considered sufficient to ensure a well-converged and well-distributed Pareto front. The analysis was performed for a representative case, the warm start-up at DNI = 900 W/m^2, and its detailed results are given in Appendix A.

The interaction between the optimisation algorithm and the transient model is illustrated in Fig. 7. The GA generates candidate decision variables, which are passed to the transient model for simulation. The resulting time histories of speed, torque, temperatures, and electrical power are post-processed to calculate the objectives and verify constraints. The GA iterates until convergence criteria are met, producing a set of Pareto-optimal start-up schedules for each operating condition.

Table 8
System constraints for the optimisation frameworks.

Parameter	Constraint	Unit
Receiver wall temperature	$T_{m,rec} < 1495$	[K]
Recuperator wall temperature	$T_{m,recu} < 923$	[K]
Turbine casing temperature	$T_{m,t} < 1173$	[K]
Compressor surge margin	$SM > 15$	[%]
Shaft rotational speed	$N < 150$	[krpm]
PMSM electrical current	$I < 15$	[Amps]
PMSM electrical power	$P_e < 6$	[kW]

2.4. Start-up scheduling

To apply the optimised schedules under time-varying irradiance, they are combined into a rule-based, DNI-scheduled speed control strategy, shown in Fig. 8. The start-up begins with a schedule selected from the cold start-up set according to the prevailing DNI. As irradiance changes, the schedule is re-selected at each DNI update from the warm start-up set, and the current stage is adjusted to the new schedule. The shaft then progresses through the stages defined in Fig. 8, holding at N_1 and N_2 for their dwell periods before accelerating to N_3. Once N_3 is reached, the system enters the operating state, in which the shaft speed follows the maximum permissible power speed for the prevailing DNI. In this way, the optimised schedules act as a look-up table that adapts the remaining start-up stages to irradiance fluctuations, such as those caused by passing clouds, without requiring any further optimisation during operation. The strategy requires only a lookup table of the parameters in Table 7, a simple stage logic and a PI speed loop, so it can run on a standard industrial controller without online optimisation. The only measurements needed are DNI, shaft speed and recuperator temperature.

Since the speed schedules were optimised for constant DNI values, in operation they are applied through a lookup table: the schedule of the DNI band containing the measured value is used. To select the width of these bands, a sensitivity analysis was carried out for DNI intervals of 200, 100 and 50 W/m^2, with the warm start-up schedule at DNI_ref = 700 W/m^2 as the reference, Fig. 9. For each interval, the schedules optimised at the band limits (DNI_ref $\pm$ Δ/2) were compared with the reference schedule. Reducing the interval from 200 to 100 W/m^2, which increases the number of schedules from 4 to 7, roughly halved the maximum deviation of the rated speed N_3 (7.9% to 3.8%) and of the end of the N_1 hold (21.1% to 10.0%), and reduced that of the generation start from 14.2% to 5.3%. A further reduction to 50 W/m^2 lowered the rated-speed deviation to 1.9% but required 13 schedules, while the deviation of the generation start increased to 7.7%. The second speed N_2 deviated by at most 3.1% for all intervals. The 100 W/m^2 interval was therefore selected as a compromise between accuracy and the number of schedules required.

3. Results and discussion

To establish a reference for subsequent optimisation, the transient

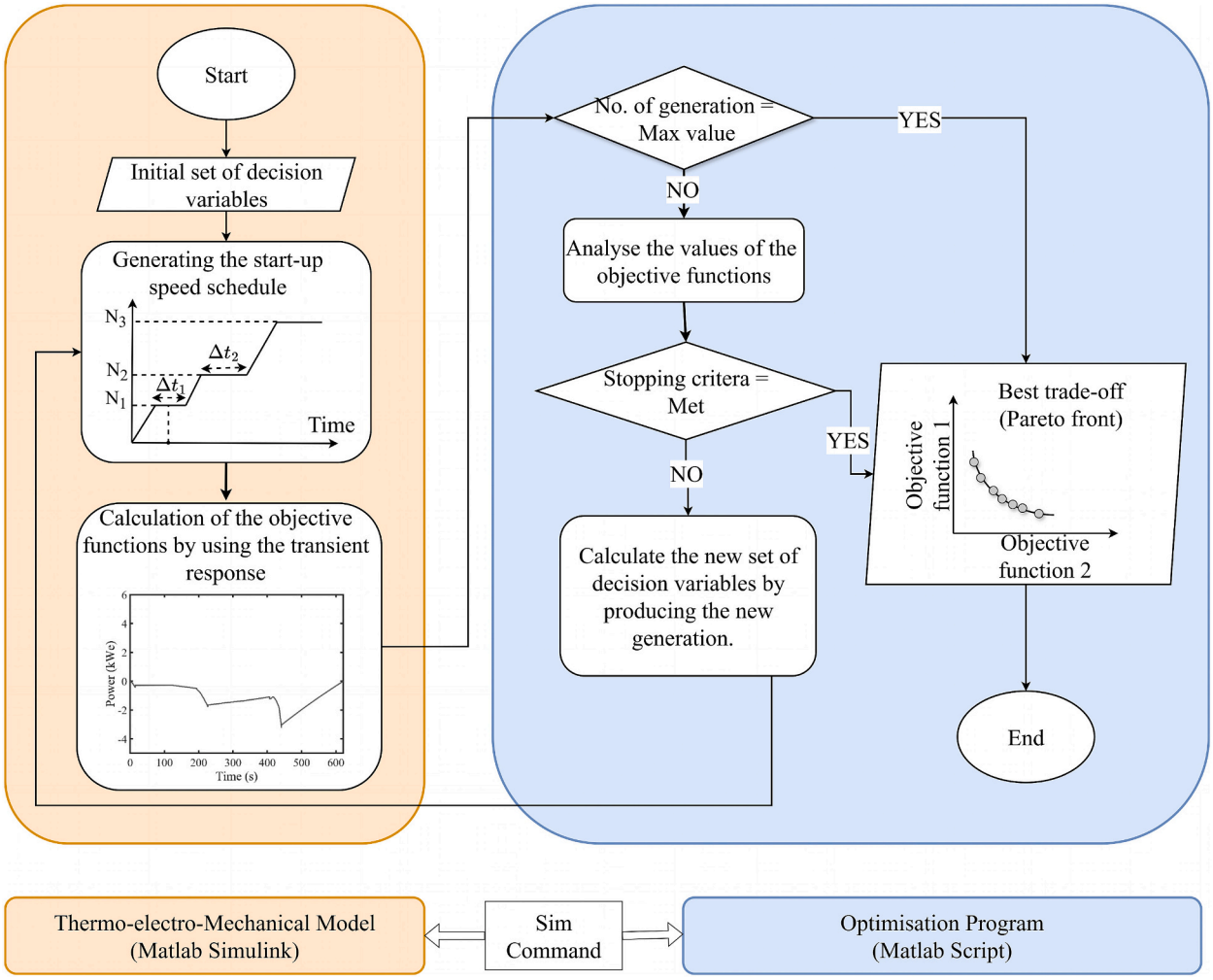


Fig. 7. Optimisation framework diagram.

response of the CSP-MGT system during a nominal, non-optimised start-up was simulated at two representative irradiance levels: 300 W/m^2 (low DNI case) and 900 W/m^2 (high DNI case). The sample schedule was the reference OMSoP start-up procedure, referring to the empirical multi-stage speed schedule used during the experimental operation of the OMSoP demonstration plant at ENEA Casaccia [18]. Given the absence of a directly comparable solar-only MGT start-up study in the literature, the empirical multi-stage OMSoP start-up procedure used during experimental operation of the demonstration plant at ENEA Casaccia [18] was adopted as the reference. Using the same 6 kWe system configuration and operating constraints provides a consistent basis for evaluating the effect of the proposed optimisation. The sample schedule was the reference OMSoP start-up procedure, referring to the empirical multi-stage speed schedule used during the experimental operation of the OMSoP demonstration plant at ENEA Casaccia [18]. That procedure consisted of fixed ramp rates and dwell times established for safe operation rather than for optimal energy use, Fig. 10-a.

Fig. 10 illustrates the transient profiles of shaft speed and electrical power for the two DNI levels. These baseline profiles correspond to the empirical start-up procedure used during the OMSoP experimental campaign [18]. It is a stepped procedure in which the shaft speed is raised in fixed 10 krpm increments (≈1 krpm/s per transition), with a hold at each step, until the DNI-dependent final speed is reached (Table 9 and Fig. 10-a). Because it was defined operationally for safe commissioning rather than as a parameterised profile, it is characterised by its step rule rather than by the decision variables used in the optimisation.

At high irradiance, receiver heating occurs rapidly, allowing the turbine inlet temperature to rise quickly and the engine to reach its rated power earlier. Under weak irradiation, the slower thermal build-up leads to extended motoring operation and high cumulative energy consumption, whereas at strong irradiation, faster acceleration increases the risk of transient overshoot if not properly controlled. Both cases therefore demonstrate that a single, fixed-rate speed ramp cannot ensure optimal or reliable performance across all solar conditions. This motivated the introduction of an optimised start-up schedule, which dynamically balances thermal, electrical, and aerodynamic constraints to minimise energy use while maintaining safe operation.

3.1. *Starter power sizing*

The first stage of the optimisation focused on determining the maximum motoring power required during start-up, which directly influences the sizing of the external starter or battery in off-grid operation. This was evaluated by performing a two-objective optimisation of maximum required power and total motoring energy consumption for a range of DNI values, using the warm start-up condition as the reference case.

Fig. 11 presents the Pareto fronts obtained for cold start-ups under different DNI levels. As expected, higher DNI values result in greater peak motoring power. This is a direct consequence of the cubic relationship between compressor work and shaft speed: for high DNI values, the final rated speed N_3 is higher than at low DNI values, increasing the compressor load during acceleration. While multiple Pareto-optimal

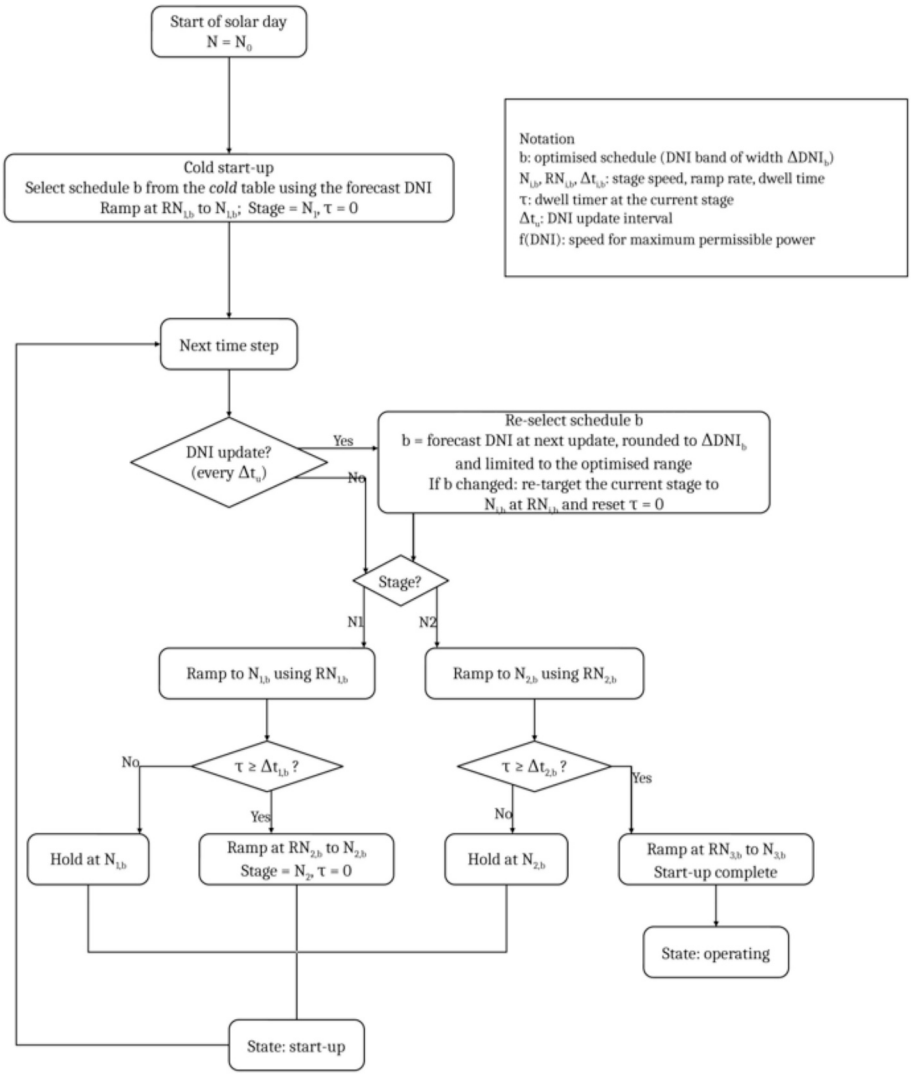


Fig. 8. DNI-scheduled speed control strategy for start-up under time-varying irradiance.

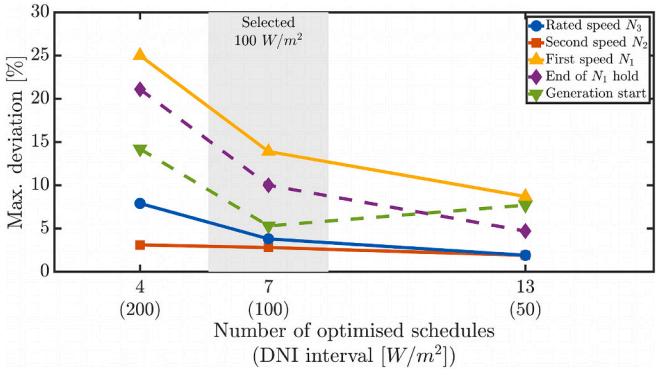


Fig. 9. Maximum deviation of the band-limit speed schedules from the 700 W/m^2 reference against the number of optimised schedules (DNI interval), with the selected 100 W/m^2 interval shaded.

schedules exist for each DNI, the starter capacity must be sized to meet the highest power requirement. In this case, the maximum peak power requirement occurs at DNI = 900 W/m^2, with a value of approximately 2 kWe. A nominal rating of 2.5 kWe was therefore considered, such that the predicted peak demand corresponds to 80% of the installed starter/drive rating, consistent with commonly adopted reliability-oriented derating practice in power electronics [45,46]. This headroom applies to the starter and associated power electronics rather than to battery sizing. For an off-grid implementation, battery selection should additionally account for ageing, temperature-dependent derating and terminal-voltage variation in accordance with the applicable battery technology and operating conditions.

It is expected that the engine needs more power to start in cold condition rather than warm condition due to the lower initial component temperatures in the cold case, which prolongs the heating phase and increases the electrical load on the drive at higher speeds. A benchmark comparison between cold and warm start-ups at DNI = 900 W/m^2 is shown in Fig. 12. The Pareto fronts have similar ranges, and the peak starter capacity requirement remains governed by the cold-start high-DNI case.

From a practical perspective, this analysis highlights that starter or battery capacity can be determined from a single "worst-case" scenario, rather than all possible DNI conditions. For the system studied here, sizing to the cold-start case at maximum expected DNI ensures adequate capacity for all other operating points. With the starter capacity established, it is used as a limiting factor in all subsequent simulations. This means that the start-up procedure would be optimised in a way to keep the maximum power in the transient response below 2.5 kWe.

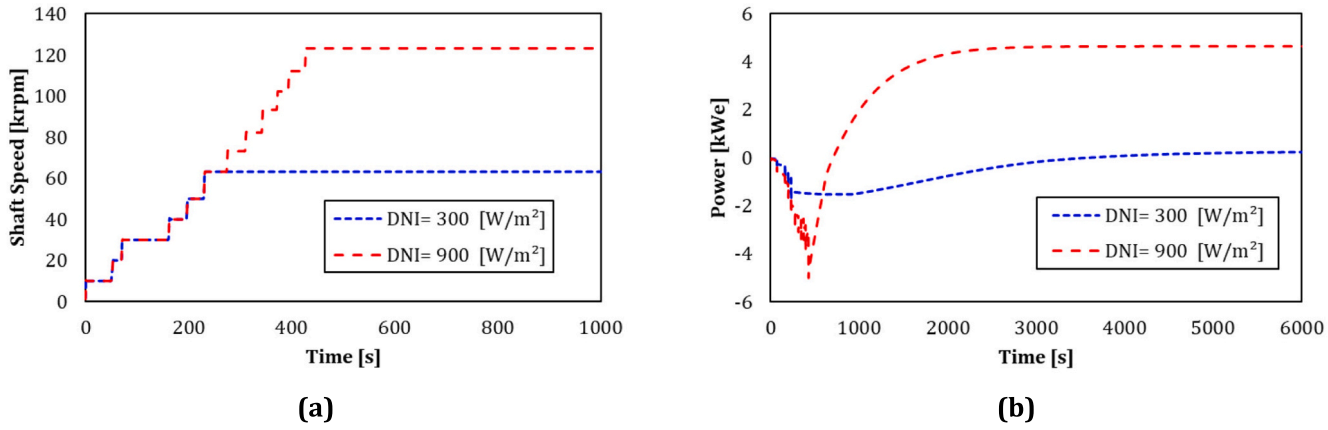


Fig. 10. Transient system behaviour during sample start-up (OMSoP start-up procedure) of the CSP-MGT system at 300 W/m^2 and 900 W/m^2: (a) Shaft speed, (b) Motoring power (negative value for power consumption).

Table 9
Baseline OMSoP start-up schedule.

Parameter	Value
Step speed	≈ 10 krpm
Transition rate	≈ 1krpm/s
Hold time per step	20 – 90s
Number of steps	6 – 12
Time to final speed	230 – 430

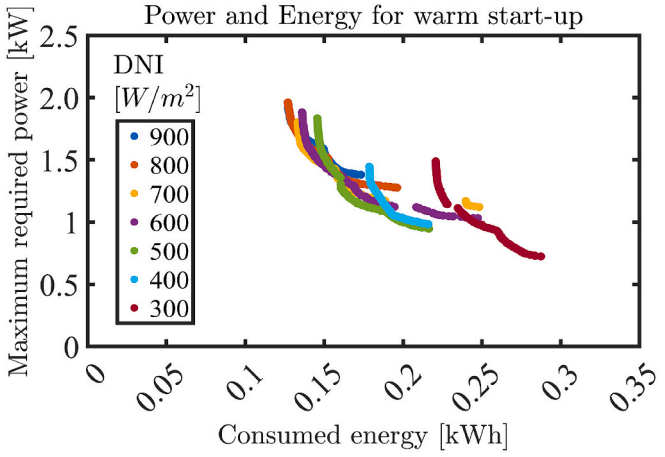


Fig. 11. Pareto fronts of multi-objective optimisation of the maximum required power and energy consumption for cold start-up.

3.2. Time–energy trade-off analysis

Once the starter capacity constraint was established another set of optimisations was performed for each DNI level and start-up scenario, producing sets of Pareto-optimal solutions representing the trade-off between total motoring energy consumption and start-up duration. Fig. 13 shows the optimisation results for warm start-ups at different DNI levels. Each plot illustrates the progression of solutions toward the final Pareto front, with a clear movement from non-dominated points scattered across the objective space to a well-defined frontier of optimal trade-offs.

Convergence was confirmed by tracking the hypervolume (HV) indicator of the Pareto front across generations, which reached 95% of its final value by around generation 15 and stabilised above 99% by generation 100 in all cases, with no significant improvement in Pareto front quality or spread observed thereafter. With a Pareto fraction of 0.35, the

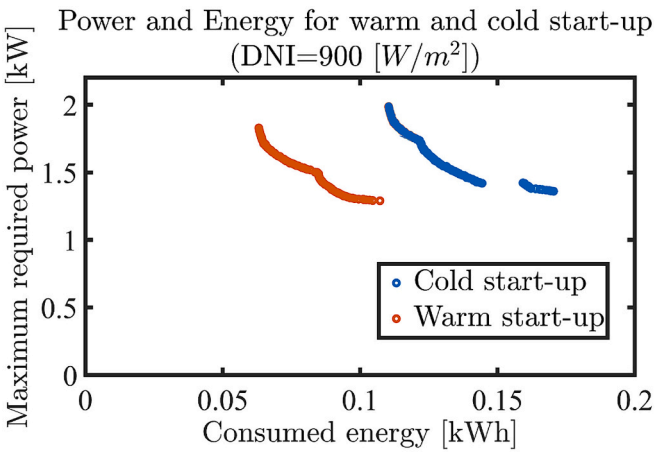


Fig. 12. Pareto fronts of multi-objective optimisation of power and energy of DNI =900 W/m2 for warm and cold start-up.

GA retains up to 105 Pareto-optimal solutions (35% of the population of 300), which are shown in the Pareto fronts. It can be observed from the provided Pareto fronts that the solutions on the frontiers are showing about 60% less energy consumption with approximately 60% less start-up time as well, compared with the average of the rest of the solutions. This means that by using the speed schedules extracted from the selected solutions on the frontier, the start-up consumed energy and start-up time could be 60% less than the potential values, which is a significant amount.

At the highest DNI (Fig. 13.a and Fig. 13.b), the Pareto front is relatively flat toward the low-energy end. At DNI = 900 W/m^2, for example, to decrease the start-up time from 520 s to 420 s (20%) the consumed energy increases by 50%. On the other hand, this indicate that reductions in motoring energy can be achieved without significantly extending start-up time. At intermediate DNI values, the trade-off becomes more pronounced, with both objectives showing a balanced sensitivity to changes in the start-up schedule parameters. For the lowest DNI (Fig. 13.g), the Pareto front steepens considerably, showing that efforts to shorten start-up time led to disproportionately high increases in motoring energy consumption. This reflects the slower heating rates at low DNI, where the receiver and recuperator require longer dwell periods to reach operational temperatures without exceeding electrical or thermal limits.

All Pareto front points in these conditions are extracted and plot with each other in Fig. 14. These differences in the shape of the Pareto fronts highlight a shift in optimisation priorities across DNI levels: at high DNI,

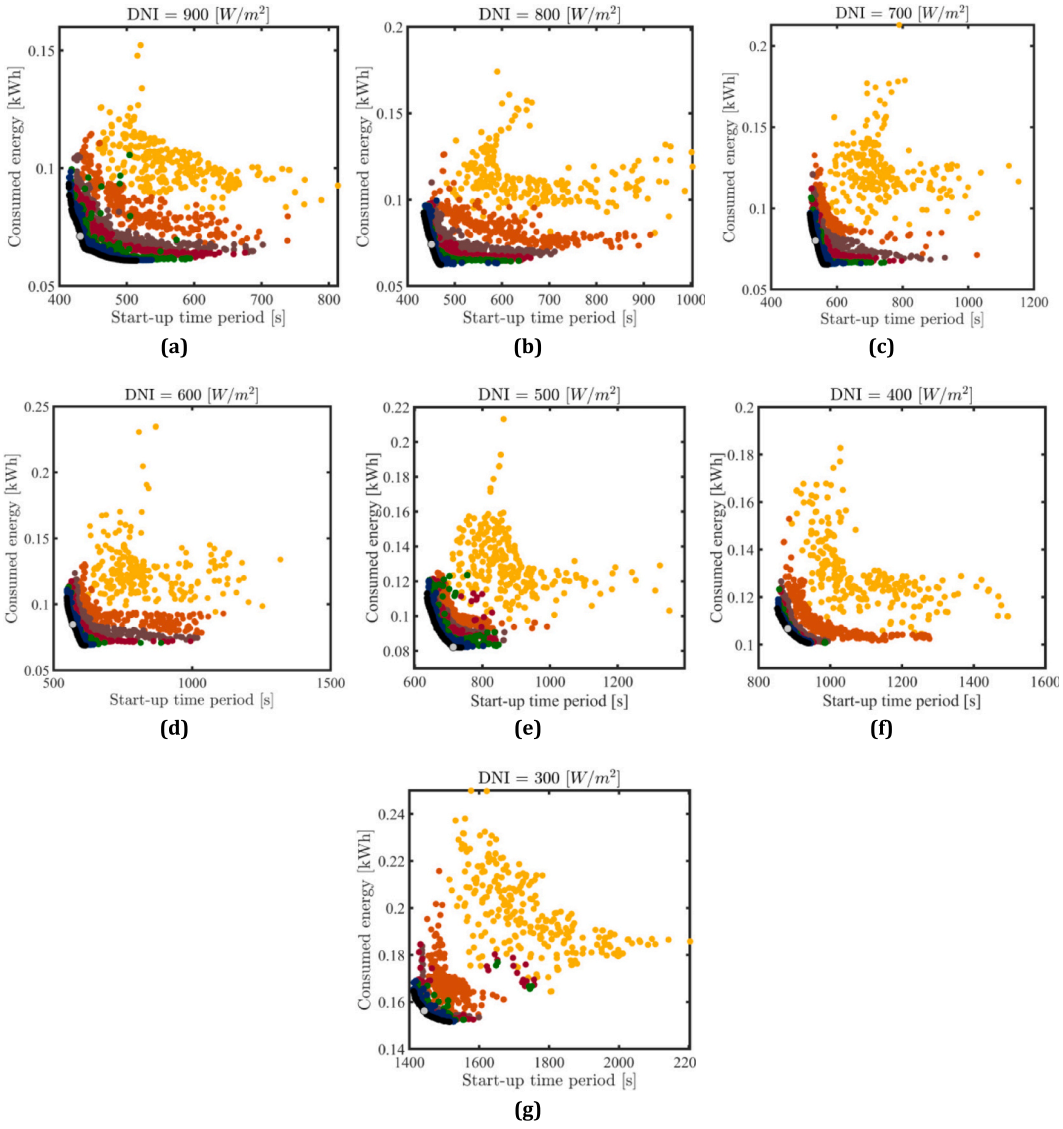


Fig. 13. Evolution of the optimisation results toward Pareto front and representative points for warm start-up under different DNI conditions: (a) 900 W/m^2, (b) 800 W/m^2, (c) 700 W/m^2, (d) 600 W/m^2, (e) 500 W/m^2, (f) 400 W/m^2, (g) 300 W/m^2.

start-up time can be reduced with only modest penalties in motoring energy, whereas at low DNI, the primary objective shifts toward minimising motoring energy, since shortening the start-up period offers little practical benefit when the overall heating duration remains inherently long.

The procedure was repeated for the warm start-up scenario in

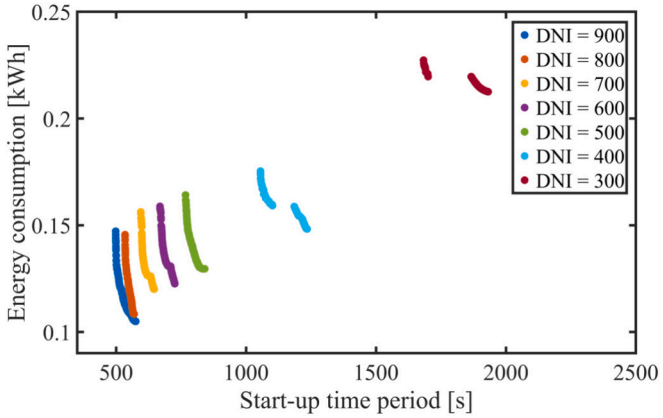


Fig. 14. Multi-objective optimisation Pareto fronts for cold start-up energy consumption and time with varying DNI values.

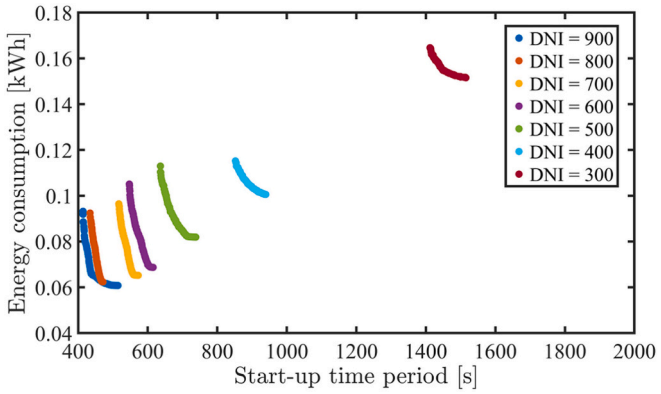


Fig. 15. Multi-objective optimisation Pareto fronts for warm start-up energy consumption and time with varying DNI values.

different DNI values. The converged Pareto fronts of these solutions are plotted in Fig. 15. Comparing cold (Fig. 14) and warm (Fig. 15) start-ups confirms that the optimised schedule takes more time and energy in cold condition.

In both cases, lower DNI values shift the Pareto fronts toward higher start-up times and greater energy consumption. This behaviour is driven by the reduced thermal input to the receiver and recuperator, which slows heating and requires longer dwell times at lower speeds to avoid exceeding acceleration or thermal limits. As a result, start-up times for DNI = 300 W/m^2 can be almost four times longer than those for DNI = 900 W/m^2, approximately 1500 s versus 400 s for warm starts.

For high DNI values ($\geq$ 800 W/m^2), the differences in start-up time between Pareto-optimal solutions can be significant, reaching up to 120 s for warm starts and 250 s for cold starts. In such cases, prioritising shorter start-up time at the expense of slightly higher energy consumption can leave more time for power generation, potentially compensating for the additional motoring energy. Conversely, at low DNI, the variation in start-up time across the Pareto front is small compared to the absolute duration of the start-up. Here, selecting the solution with minimum motoring energy consumption is more advantageous, as the extra time saved by faster schedules has negligible impact on daily energy yield.

The energy consumed during start-up across all cases ranges from 0.06 to 0.24 kWh. For DNI = 300 W/m2, the start-up energy can even exceed the amount of energy the system could have generated at the same time at full load, underscoring the importance of efficient scheduling under low solar input conditions.

3.3. Parameter trends and operational guidance

For further comparative analysis, a single representative solution was selected from the Pareto front for each DNI level and start-up type. The selection was based on an energy-based criterion that accounts for the potential benefit of earlier power generation. This allows the trade-off between the two objectives to be evaluated using a common physical quantity, namely energy. For each Pareto solution, a modified motoring energy (E_{mod}) was calculated as eq. (30).

$$E_{mod} = E_{start} - E_{gen,\Delta t} \tag{30}$$

where E_{start} is the motoring energy consumed during start-up and $E_{gen,\Delta t}$ is the potential electrical energy that can be generated as a result of reaching the self-sustaining operating condition earlier, which is calculated as eq. (31).

$$E_{gen,\Delta t} = \int_{t_{start}}^{t_{start}+\Delta t} P_e(t)\, dt \tag{31}$$

The corresponding time advantage is defined as $\Delta t = t_{max} - t_{start}$, where t_{max} is the maximum start-up time among the solutions on the same Pareto front and t_{start} is the start-up time of the solution being evaluated. Thus, a solution requiring greater motoring energy is favoured only when the potential generation benefit associated with its shorter start-up time compensates for that additional energy requirement.

The modified motoring energy was evaluated for all solutions on each Pareto front, and the solution with the minimum E_{mod} was selected as the representative operating point for subsequent comparisons. Because the generation credit $E_{gen,\Delta t}$ depends on the available solar input, the same criterion naturally reflects different operational priorities under different DNI conditions. At lower DNI, the benefit of earlier generation is smaller, and the selected solution tends toward an energy-saving priority, whereas at higher DNI the increased generation potential places greater value on reducing start-up duration, corresponding to a power-generation priority. The selected points are indicated in grey in Fig. 13 and their values are reported in Table 10.

Fig. 16 illustrates the speed schedules corresponding to the selected Pareto-optimal points, showing the focusing moment and the onset of power generation in each case. The optimised start-up procedure consistently exhibits a distinctive multi-stage structure rather than a single continuous ramp. A single-ramp profile was not found to be feasible in any optimisation outcome. At high acceleration rates, the solar receiver does not receive sufficient time to accumulate thermal energy, forcing the electric drive to supply most of the input power and risking an exceedance of the current limit. Consequently, even at low DNI values, where the rated speed is lower than the drive's capacity, the optimiser still converges to multi-stage rather than single- or two-ramp profiles.

In all optimised schedules, the dish focusing begins very early in the start-up phase, almost immediately after the shaft reaches N_1, with only a few-seconds delay in some cases. This timing is consistent across both warm and cold start-ups and across all DNI levels. The first dwell period, Δt_1, during which the shaft speed remains constant at N_1, is equal to or longer for cold start-ups compared with warm cases. A similar pattern is observed for the second dwell time, Δt_2, at N_2, reflecting the additional thermal inertia of the colder system. Another important observation is that the self-sustaining point is consistently reached at the rated speed in all scenarios. This behaviour contrasts with that of fuelled micro gas turbines, where self-sustainment typically occurs below the rated value. The difference arises from the control principle of solar-only CSP-MGTs, in which the shaft speed is directly commanded rather than indirectly governed through fuel flow. As a result, when power generation begins at a speed below the rated value, the system must subsequently accelerate to the designated operating speed, requiring additional electrical power input. Also, the onset of power generation occurs later in cold start-ups than in warm ones for all DNI levels, due to the longer time required to pre-heat thermal components.

To illustrate the direct effect of the optimisation on transient power behaviour, Fig. 17 shows a comparison of the electrical power profiles obtained from the baseline OMSoP start-up schedule and the optimised schedule for two representative irradiance levels. At DNI = 300 W/m^2, shown in Fig. 17.a, the optimised schedule utilises the higher motoring power capacity, reducing the cumulative motoring energy requirement by more than 35%. The longer focus period limits power fluctuations and avoids unnecessary current draw during the early stages of heating. At DNI = 900 W/m^2, Fig. 17.b, both schedules reach the self-sustaining point within approximately 700 s, but the optimised case achieves this with reduced overshoot and earlier transition to generation mode, reducing the cumulative motoring energy requirement by more than 25%. These results demonstrate that the optimised schedule not only decreases total energy consumption but also mitigates instantaneous power demand and fluctuations.

The motoring energy consumption of the selected solution points for cold and warm start-ups across different DNI levels is shown in Fig. 18 and Fig. 19, both in absolute terms and as a fraction of the potential

Table 10
Energy consumption and start-up time for the selected solution at each DNI.

		DNI [W/m2]						
		900	800	700	600	500	400	300
Warm	E_{start} [kWh]	0.071	0.074	0.080	0.085	0.082	0.107	0.156
start-up	t_{start} [s]	431	451	535	570	714	882	1443
Cold	E_{start} [kWh]	0.122	0.125	0.136	0.140	0.146	0.159	0.220
start-up	t_{start} [s]	514	544	603	680	781	1102	1701

energy generation. In both cases, higher DNI requires less motoring energy in both absolute and relative metrics. This is primarily due to the faster heating of the receiver and recuperator under higher solar input, which shortens the dwell periods at intermediate speeds and reduces the total time spent in motoring mode. At the lowest DNI of 300 W/m^2, however, the motoring energy required for start-up can exceed the amount of energy the system could produce during the same period at full load. This implies that initiating start-up under such low irradiance conditions could result in a net energy loss unless the system remains in generation mode for a sufficiently long period afterwards to offset the initial cost. For this reason, operation at very low DNI should be carefully managed, and in some cases avoided, if it is unlikely that the system can achieve a net positive energy yield over the course of the day.

The normalised values of the four key parameters defining the optimised start-up schedules, N1/N3, N2/N3, Δt1/tstart, and Δt2/tstart, are presented in Fig. 20 for both warm and cold start-ups across the full range of DNI inputs. The first-stage speed, N_1, the focus speed at which the dish begins directing radiation toward the receiver, remains largely constant in absolute terms, averaging about 17 krpm with minimal variation. When normalised by the rated speed, however, N_1/N_3 decreases with increasing DNI. This behaviour arises because higher solar input permits higher rated speeds, while the initial acceleration point remains constrained primarily by aerodynamic and electrical factors rather than by final power output.

The second-stage speed N_2, with average value of 72% for cold start-up and 87% for warm start-up, shows greater variability with DNI, reflecting its key role in balancing the competing objectives of start-up duration and motoring energy. Warm start-ups exhibit slightly higher N_2/N_3 values than cold ones, consistent with their lower heating requirements. Higher N_2 levels shorten the overall start-up but at the cost of increased compressor work, which rises approximately with the cube of speed.

The first dwell period, Δt_1, constitutes the dominant portion of the start-up schedule, accounting for roughly 60–80% of the total duration for both start-up types. Its fraction peaks around mid-range DNI, where the balance between available thermal input and heating requirement is most favourable. This extended dwell ensures adequate heating of the receiver and recuperator before subsequent acceleration. The second dwell time, Δt_2, is consistently shorter but exhibits a complementary trend to Δt_1, decreasing at mid-range DNI and increasing again toward lower and higher irradiance levels. This inverse pattern confirms that the optimiser redistributes the total dwell duration between the two stages to balance receiver heating and electrical acceleration limits across varying solar inputs.

The results provide both a quantitative and qualitative basis for operational decision-making. The consistent values of N_1 and the proportionally long Δt_1 suggest that certain aspects of the start-up schedule can be standardised for a given system configuration, simplifying control implementation. Meanwhile, the sensitivity of N_2 and the overall trade-off between time and energy consumption with varying DNI highlight the need for adaptive control strategies that can tailor acceleration profiles to real-time operating conditions. The finding that start-up under very low DNI may not yield a net energy gain underscores the importance of incorporating irradiance forecasts and expected generation windows into start-up scheduling decisions.

Using the discrete optimised start-up schedules identified at DNI intervals of 100 W/m^2, a complete start-up strategy for the CSP-MGT system can be defined, in which the schedule of the DNI band containing the measured value is applied. This strategy was subsequently applied to assess the annual performance of the system under transient operating conditions, as presented in the following section.

3.4. Annual performance assessment

A direct quantitative comparison with published solar-only CSP-MGT start-up studies is not currently possible, as no study identified in the available literature reports both start-up duration and motoring-energy consumption for a comparable purely solar MGT system. The empirical OMSoP start-up procedure is therefore adopted as the quantitative benchmark in the present study. Since both the reference and optimised schedules are evaluated using the same 6 kWe system model, component characteristics and operating constraints, this comparison isolates the effect of the proposed start-up optimisation without introducing differences in machine scale, receiver design or control architecture.

To evaluate the broader operational impact of the optimised start-up schedules, an annual simulation of the CSP-MGT system was conducted using minute-resolved meteorological data for the OMSoP demonstration site in Casaccia, Italy [18]. The purpose of this analysis was to quantify how the transient start-up penalties identified in the preceding sections affect annual net electricity generation, and to compare the optimised start-up strategy with the reference OMSoP start-up procedure and a quasi-steady annual estimate.

Fig. 21 illustrates the variation of DNI over a representative year at the Casaccia site, showing the distinct seasonal changes in solar input that determine the system's operating regime. The meteorological inputs were obtained from the SoDa database (extracted from [47,48]) and included DNI, ambient temperature, ambient pressure, and relative humidity.

Start-up was initiated only when the available DNI exceeded the minimum feasible start-up threshold of 260 W/m^2. This threshold was derived from the steady-state performance of the system at a DNI of 260 W/m^2, the steady-state net electrical power output of the CSP-MGT at its maximum permissible power operating point falls to zero. Below this value, the system cannot generate net positive power even after start-up is complete. If DNI subsequently fell below this threshold, the system entered a controlled shutdown and cool-down mode, during which the PMSM maintained the shaft at the minimum rotational speed of 17.5 krpm to sustain airflow through the engine while the component thermal states evolved. The start-up type was determined from the recuperator mean wall temperature. If DNI recovered to 260 W/m^2 or above while $T_{rec} \geq 393\ K$, the event was classified as a warm start; otherwise, if $T_{rec} < 393\ K$, the subsequent event was classified as a cold start. The corresponding DNI-dependent optimised start-up schedule, duration and motoring-energy requirement were then applied. The complete annual operating logic, including shutdown, cool-down and warm/cold restart classification, is summarised in the flowchart shown in Fig. 22. Using this logic, 551 start-up events were identified over the simulated year, of which 546 proceeded to the operating state.

To verify that the operating constraints are respected under realistic irradiance, the DNI-scheduled speed control strategy described in Section 2.4 was applied to two representative days of each month, for all

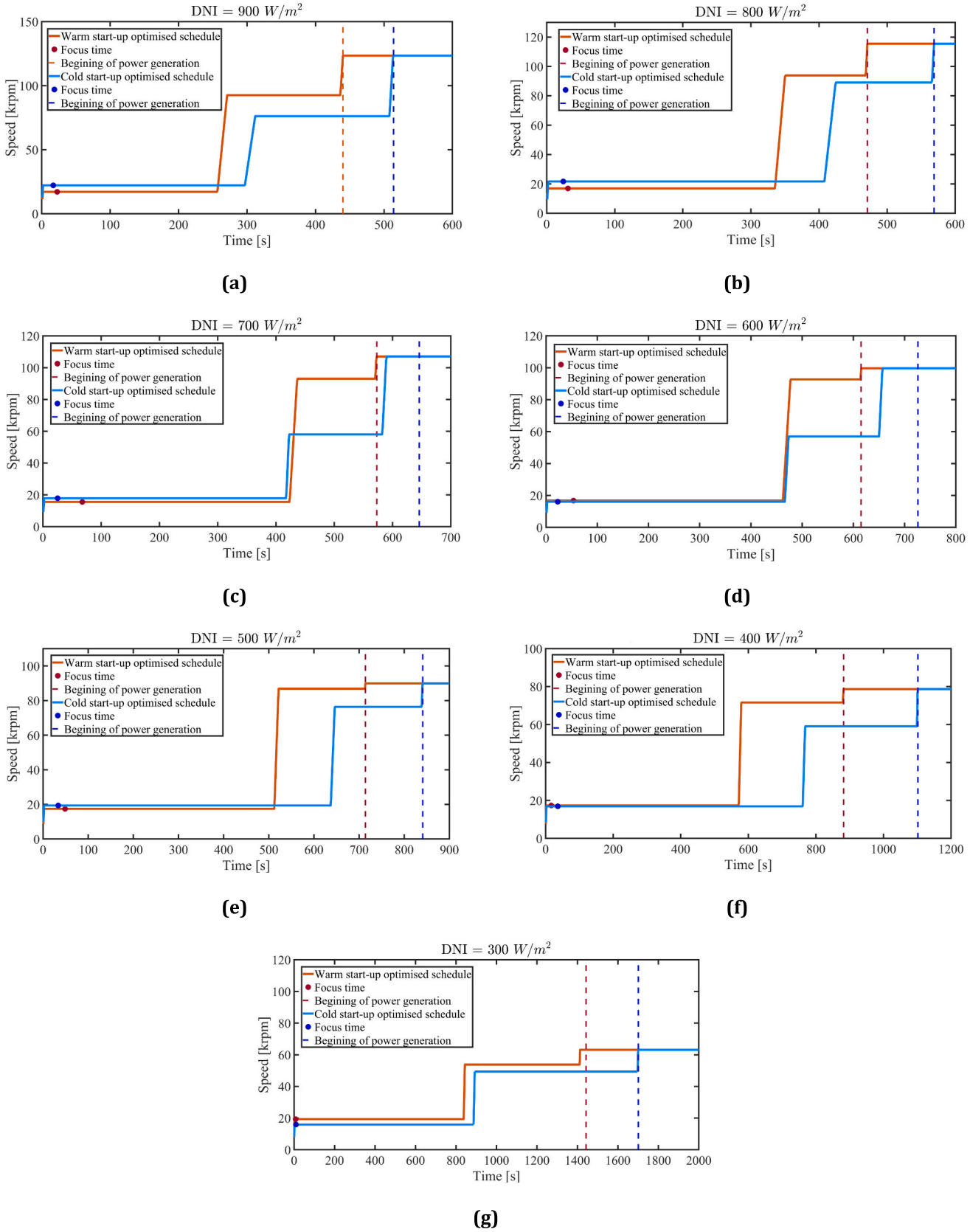


Fig. 16. Optimised speed schedules for both warm and cold start-ups under different DNI conditions: (a) 900 W/m^2, (b) 800 W/m^2, (c) 700 W/m^2, (d) 600 W/m^2, (e) 500 W/m^2, (f) 400 W/m^2, (g) 300 W/m^2.

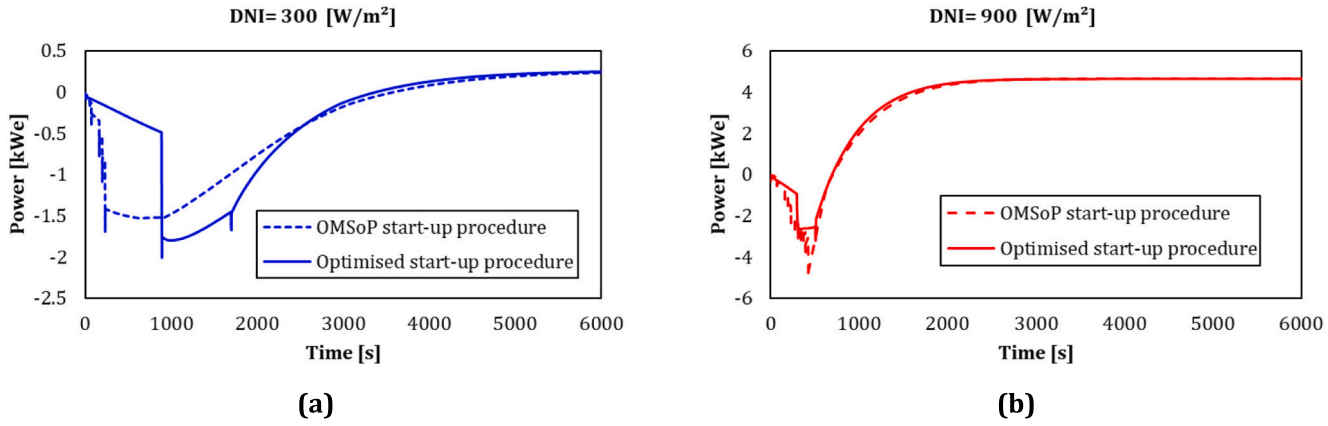


Fig. 17. Comparison of transient power evolution during start-up for the OMSoP and optimised schedules at two representative irradiance levels: (a) DNI = 300 W/m^2 and (b) DNI = 900 W/m^2.

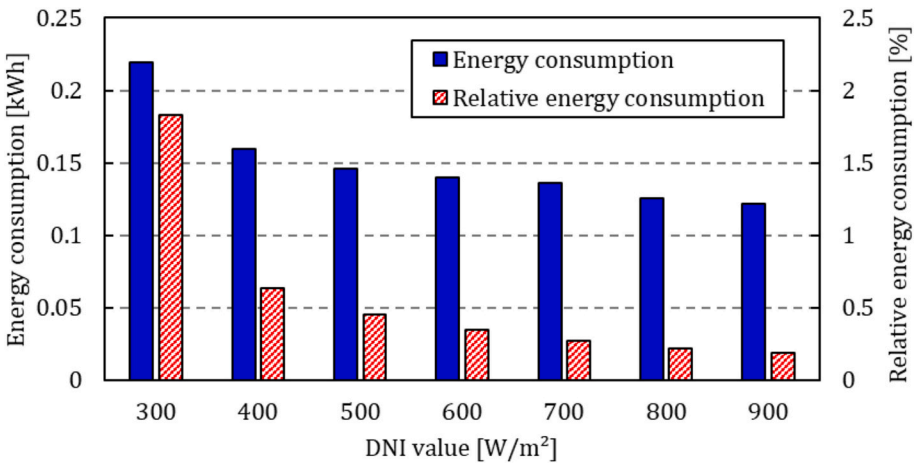


Fig. 18. Consumed energy during a cold start-up for different DNI values in two absolute and relative forms.

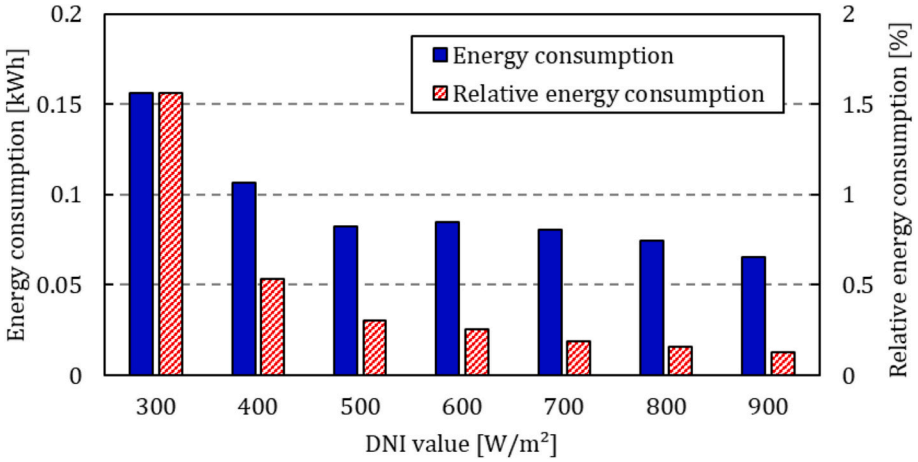


Fig. 19. Consumed energy during a warm start-up for different DNI values in two absolute and relative forms.

months using the minute-resolved DNI data for the Casaccia site. The optimised schedules were applied through a lookup table with DNI intervals of 100 W/m^2: at each DNI update, the schedule of the band containing the measured DNI was selected. Fig. 23 show all operating points on the compressor map, together with the metal temperatures and the PMSM current against their limits. No temperature, surge-margin, current or speed constraint was violated. All operating points lay on the stable side of the 15% surge-margin line, with a minimum surge margin of 30.2%. The maximum receiver wall, turbine casing and recuperator wall temperatures were 1381 K, 1017 K and 651 K, below their limits of 1495 K, 1173 K and 923 K, respectively. The PMSM current did not exceed 15 A. During start-up, the constraints are respected

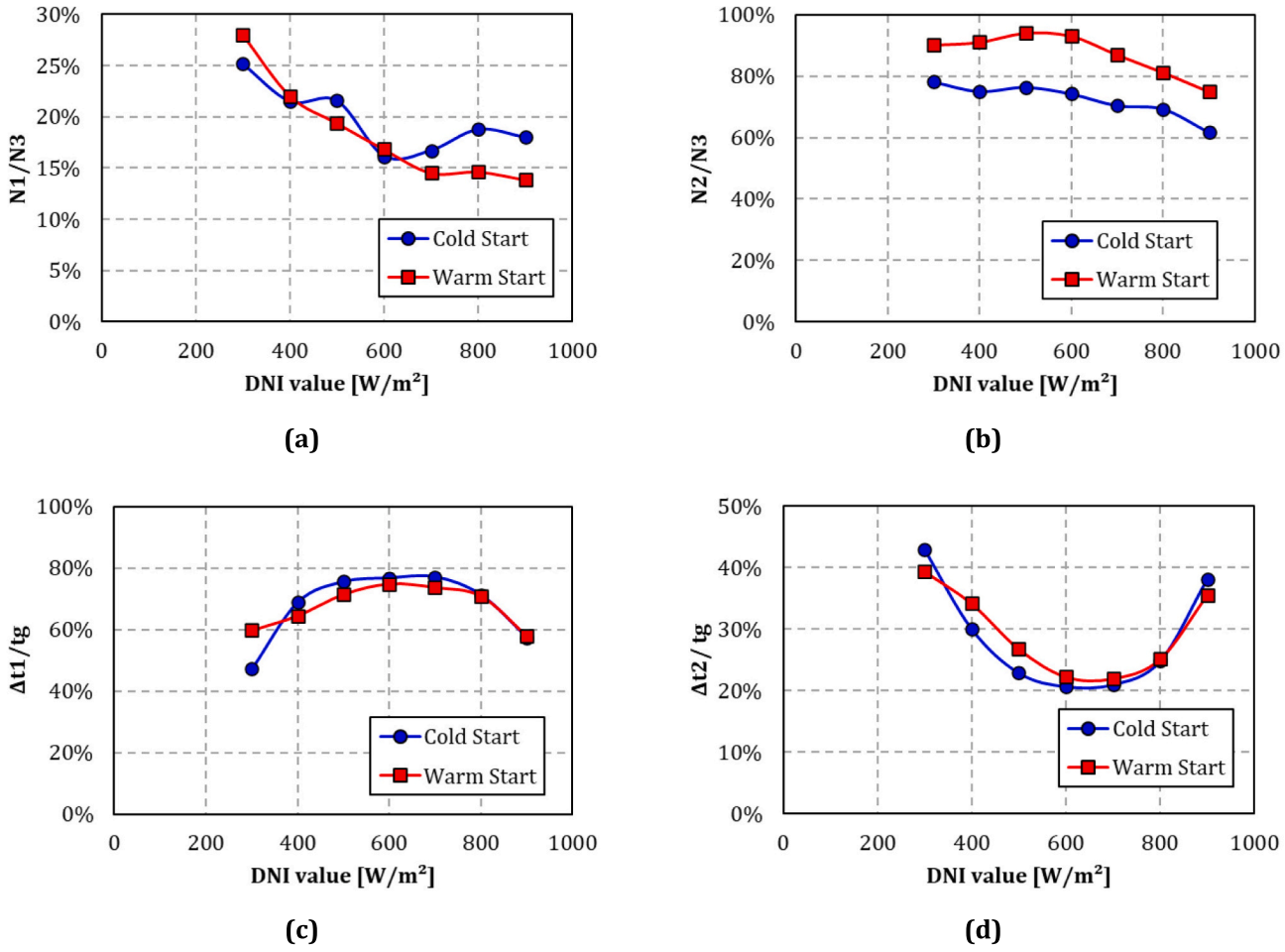


Fig. 20. Normalised values of the four main parameters of the optimised start-up schedules for warm and cold start-up modes across different DNI levels: (a) N_1/N_3, (b) N_2/N_3, (c) $\Delta t_1/t_{start}$, (d) $\Delta t_2/t_{start}$.

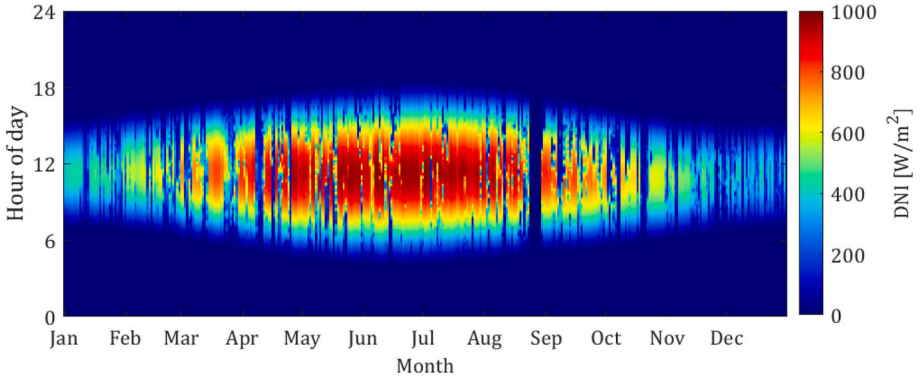


Fig. 21. Annual variation of direct normal irradiance (DNI) at the Casaccia (Italy) site.

because each schedule was optimised with these constraints imposed, and re-selection at each DNI update keeps the applied schedule matched to the prevailing DNI band. During generation, the shaft follows the maximum power point speed, at which all temperatures remain within their limits.

The optimised schedules were applied as discrete schedules at DNI intervals of 100 W/m^2 (300, 400, …, 900 W/m^2): at each DNI update, the schedule of the DNI band containing the measured value was applied (Section 2.4). For DNI values between 260 and 300 W/m^2, the schedule corresponding to 300 W/m^2 was applied, while for DNI values above 900 W/m^2, the schedule corresponding to 900 W/m^2 was used. The system was shut down when the generated power became insufficient to sustain operation. The same operating criterion was applied to both the reference OMSoP schedule and the optimised schedule to ensure a consistent comparison. Since P_e is treated as positive during generation and negative during motoring, the annual net energy was obtained by integrating P_e over time, while the start-up energy consumption was calculated from the magnitude of the negative motoring contribution.

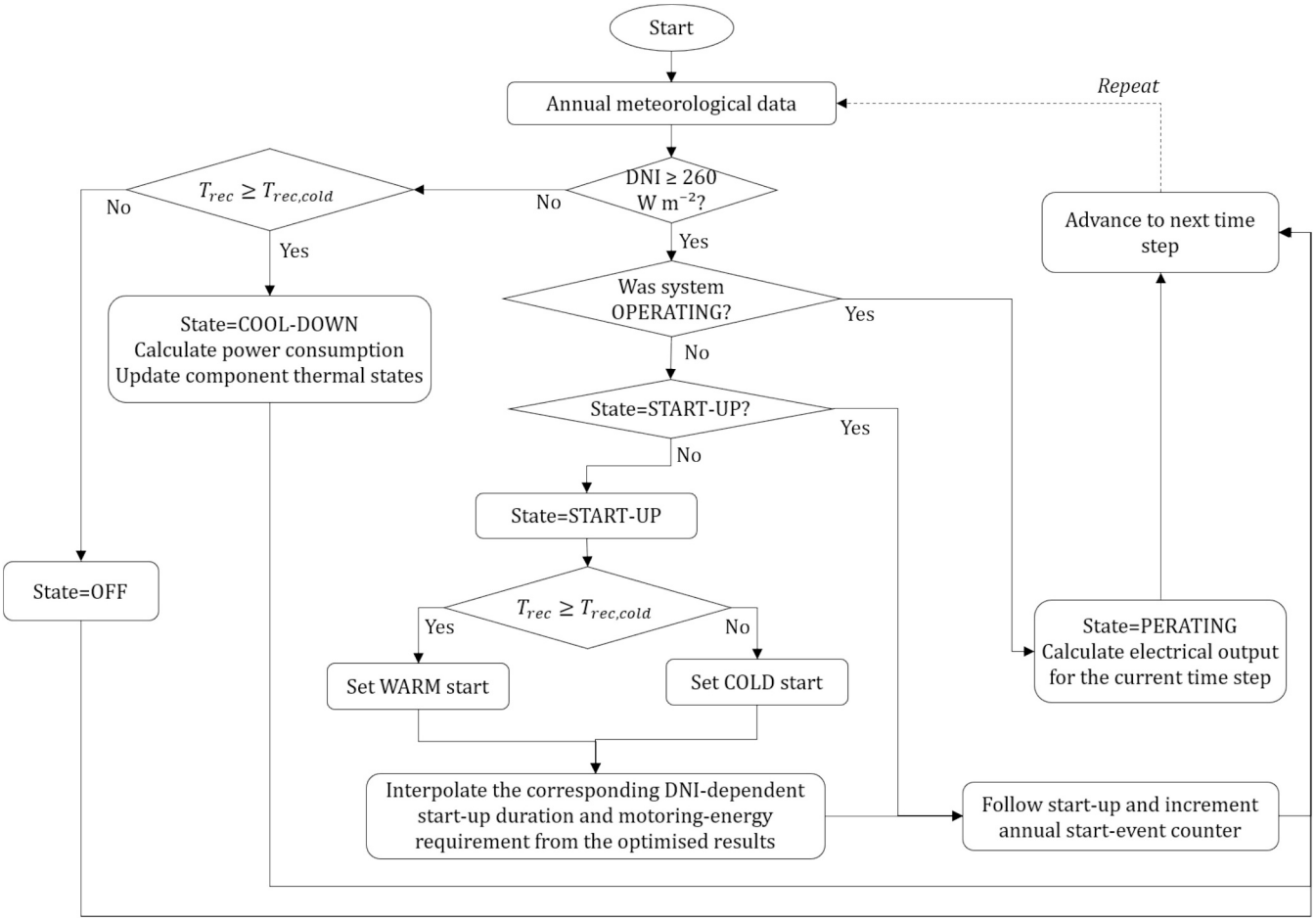


Fig. 22. Annual performance assessment flowchart.

The energy consumed during start-up was compared for the two cases using the reference OMSoP and the optimised speed schedules across all DNI values, as shown in Fig. 24. The results clearly indicate that adopting the optimised schedules reduces start-up energy consumption by approximately 30–60% relative to the reference procedure. This improvement arises from the shortened dwell periods and smoother acceleration profile of the optimised strategy, which limit unnecessary compressor work during early transients.

Fig. 25 presents the annual energy balance of the CSP-MGT system, comparing the cumulative start-up energy consumption and total net electricity generation obtained from the transient simulations with a quasi-steady estimation that neglects dynamic effects. The quasi-steady model overestimates annual generation by ignoring transient losses and component thermal inertia, predicting 7.53 MWh compared with 7.20 MWh for the optimised schedule and 6.84 MWh for the baseline OMSoP schedule. When dynamic effects are considered, start-up losses alone account for roughly 7% of the total annual energy generation in the baseline case and about 3% when the optimised procedure is applied. The remaining discrepancy with the quasi-steady results arises from transient phenomena occurring during normal operation, such as recuperator/receiver heating.

The comparison highlights the importance of employing a coupled transient electro-thermo-mechanical model, as it captures the real physical constraints and energy penalties that are otherwise overlooked in quasi-steady analyses. Collectively, the findings confirm that the proposed optimisation framework enhances the operational viability of solar-only CSP-MGT systems by minimising start-up penalties while preserving reliability, an essential step toward continuous, dispatchable solar power generation.

Beyond the start-up performance considered here, the practical value of solar-only CSP-MGT systems depends strongly on their application context. Eliminating fuel consumption and hybridisation equipment can simplify the system and reduce investment and maintenance requirements relative to hybrid configurations. While economic performance improves with increased production volume, their competitiveness remains site- and scale-dependent, and the levelised cost of electricity can remain higher than that of mature photovoltaic technologies at low production volumes [2]. These characteristics indicate that solar-only CSP-MGT systems are most attractive in applications where fuel independence and local generation are important, particularly in remote or less-developed locations with favourable solar resources. For such applications, the frequent start-stop operation inherent to solar-only systems makes the reduction of start-up energy consumption and duration demonstrated in the present study directly relevant to overall system viability.

4. Conclusions

This study employed a validated transient electro-thermo-mechanical model of a solar-only micro gas turbine system to optimise the start-up process under varying solar irradiance conditions. The model integrated thermodynamic, electrical, and control subsystems within a coupled framework, capturing the dynamic interactions that govern start-up behaviour.

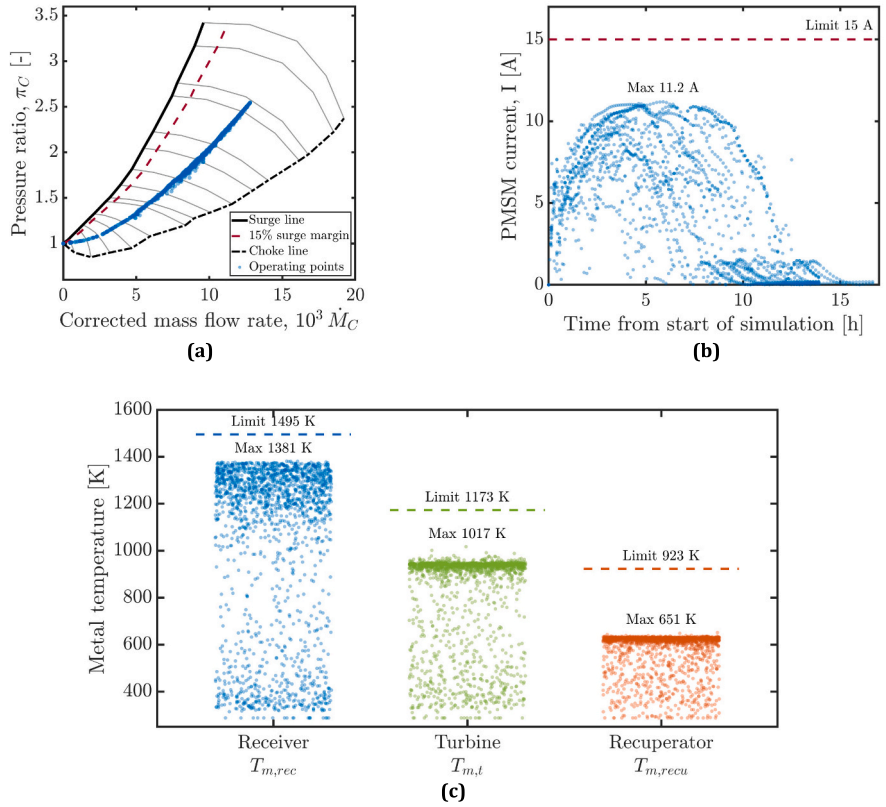


Fig. 23. Operating points of all simulated days the operating constraints: (a) compressor map with the surge line and the 15% surge-margin line, (b) PMSM current, (c) receiver, turbine casing and recuperator metal temperatures.

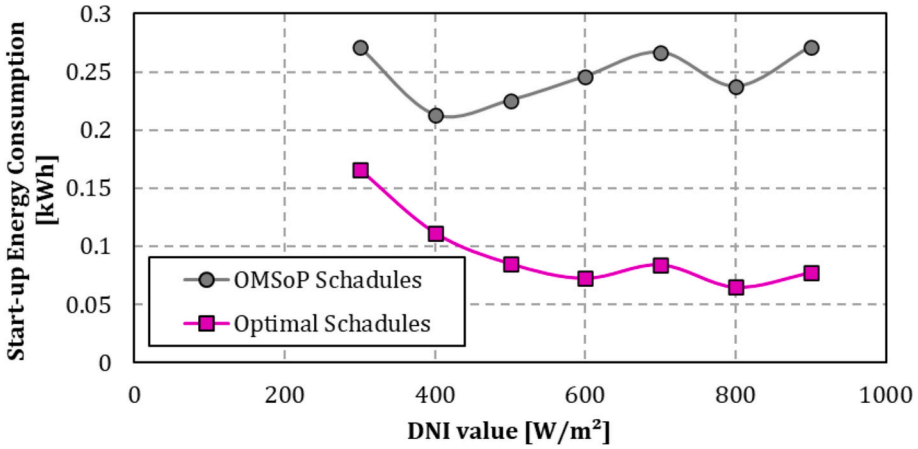


Fig. 24. Comparison of start-up energy consumption between the reference OMSoP speed schedules and the optimised start-up schedules across different DNI values.

A multi-objective optimisation framework was employed to minimise both start-up time and motoring energy consumption while satisfying system constraints, including surge margin, electrical current limits, and component temperature thresholds. The results show that the optimal start-up trajectory consistently adopts a multi-stage speed schedule comprising two dwell periods, enabling effective receiver heating and thermal stabilisation prior to power generation. The first dwell period accounted for up to 80% of the total start-up time, highlighting its dominant role in system heating dynamics. Across all DNI levels, the optimised schedules reduced start-up energy consumption by 30–60% compared with the reference OMSoP procedure, which can reduce the required motoring energy and support lower external starter/battery sizing requirements.

When implemented in a year-long simulation using site-specific solar data from the demonstration site, the optimised schedules yielded tangible operational benefits. The annual start-up losses were reduced

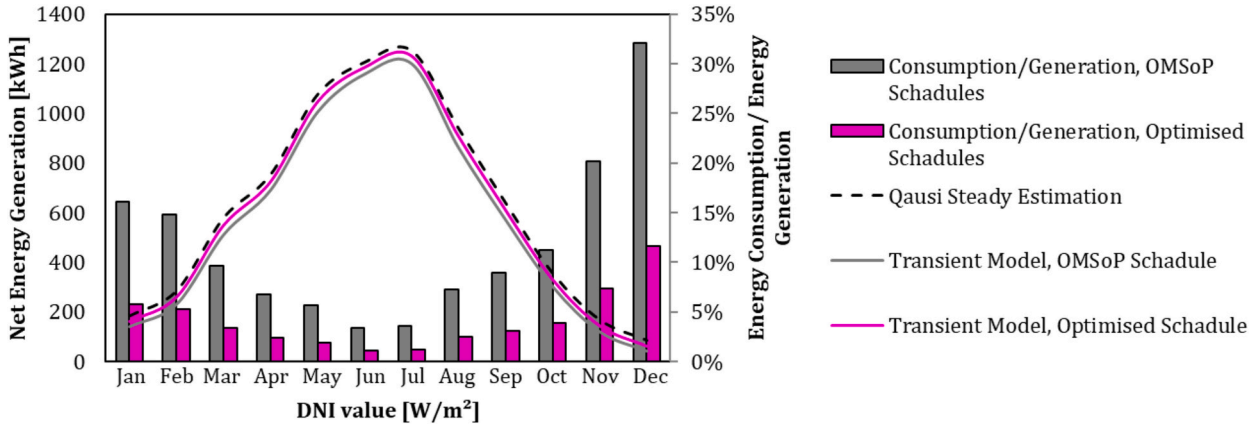


Fig. 25. Annual energy balance of the CSP-MGT system at Casaccia (Italy), comparing net energy generation and start-up energy consumption.

from approximately 7% to 3% of the total energy production, resulting in a 5.3% increase in net annual generation compared with the OMSoP default schedule for the baseline case. These results confirm that the start-up phase, although frequent in solar-only systems, imposes only a minor energy penalty when properly optimised. Moreover, comparison with a quasi-steady estimation demonstrated that transient effects, such as thermal inertia and delayed receiver response, must be considered to obtain accurate performance predictions. These operational improvements are particularly relevant to remote and distributed solar-only applications, where fuel independence is valued and repeated start-stop cycling can otherwise impose a significant energy penalty.

Overall, the proposed framework establishes a robust and transferable methodology for transient modelling and start-up optimisation of thermally driven micro power systems with appropriate model adaptation. While it has been demonstrated here for a solar-only CSP-MGT configuration, the same approach can be extended to a wide range of distributed energy technologies, including hybrid gas–solar systems, thermal energy storage units, and micro-scale combined heat and power (CHP) plants, where coupled electro-thermal dynamics and start-up behaviour critically influence performance. Beyond this specific application, the developed model and optimisation structure provide a foundation for model-based control co-design and real-time operational optimisation in renewable-driven microgeneration systems. Future research will focus on generalising the framework for off-design ambient conditions, integrated energy management, and hybridised solar-fuel architectures, supporting the transition toward flexible and dispatchable low-carbon power technologies.

Declaration of competing interest

The authors declare that they have no known competing financial interests or personal relationships that could have appeared to influence the work reported in this paper.

Acknowledgement

The first author gratefully acknowledges the financial support provided by the City *St* George's, University of London Doctoral Scholarship.

Appendix A. Sensitivity of the Pareto front to the GA population size

To verify that the optimisation results are not affected by the choice of the GA population size, the first-stage optimisation (maximum required power and consumed energy, Section 3.1) was repeated for a representative case, the warm start-up at DNI = 900 W/m^2, with eleven population sizes: 30, 80, 100, 125, 150, 175, 200, 225, 250, 275 and 300. All other GA settings were kept as described in Section 2.3.5, i.e. a crossover fraction of 0.8 with scattered crossover, adaptive feasible mutation, a Pareto fraction of 0.35 and a function tolerance of 1×10^{-4}.

Both objectives were normalised to the range [0,1] using the minimum and maximum values obtained over all runs. Each Pareto front P was then evaluated with two standard quality indicators. The hypervolume HV(P) is the area of the normalised objective space that is dominated by P and bounded by the reference point (1.1, 1.1); a larger HV indicates a front that lies closer to the ideal point and covers a wider range of trade-offs. The inverted generational distance measures how closely P approximates a reference front R, (eq. A1):

$$IGD(P) = (1/|R|)\ \Sigma_\{r \in R\}\ min_\{p \in P\}\ \|r - p\| \tag{A.1}$$

where R is the set of non-dominated solutions of all runs combined, $|R|$ is the number of solutions in R, and $\|\cdot\|$ is the Euclidean distance in the normalised objective space. A smaller IGD indicates a front that lies closer to the best known solutions and covers them without large gaps. HV is reported as a percentage of the hypervolume of R.

The results are shown in Fig. A1. Small populations produced sparse fronts far from the reference front: with 30 individuals, the front contained only 9 distinct solutions, with HV = 52.7% and IGD = 0.286. Between 30 and 125 individuals, HV increased by 37 percentage points and IGD decreased by 80%. Beyond 125 individuals, however, HV remained at 86 ± 4% and IGD at 0.086 ± 0.037 (mean ± standard deviation), with no statistically significant trend with population size (linear regression, $p = 0.93$ for HV and $p = 0.80$ for IGD). The remaining variation in this range therefore reflects the stochastic nature of the GA rather than a dependence on the population size. A population of 300, which lies within this plateau, gave the highest HV (93.2%) and the lowest IGD (0.032) of all cases, with 103 distinct solutions spread across the power–energy trade-off. Since the computational cost increases linearly with the population size, a population of 300 was considered sufficient to ensure a well-converged and well-distributed Pareto front at an acceptable computational cost, and it was used for all optimisations in this study.

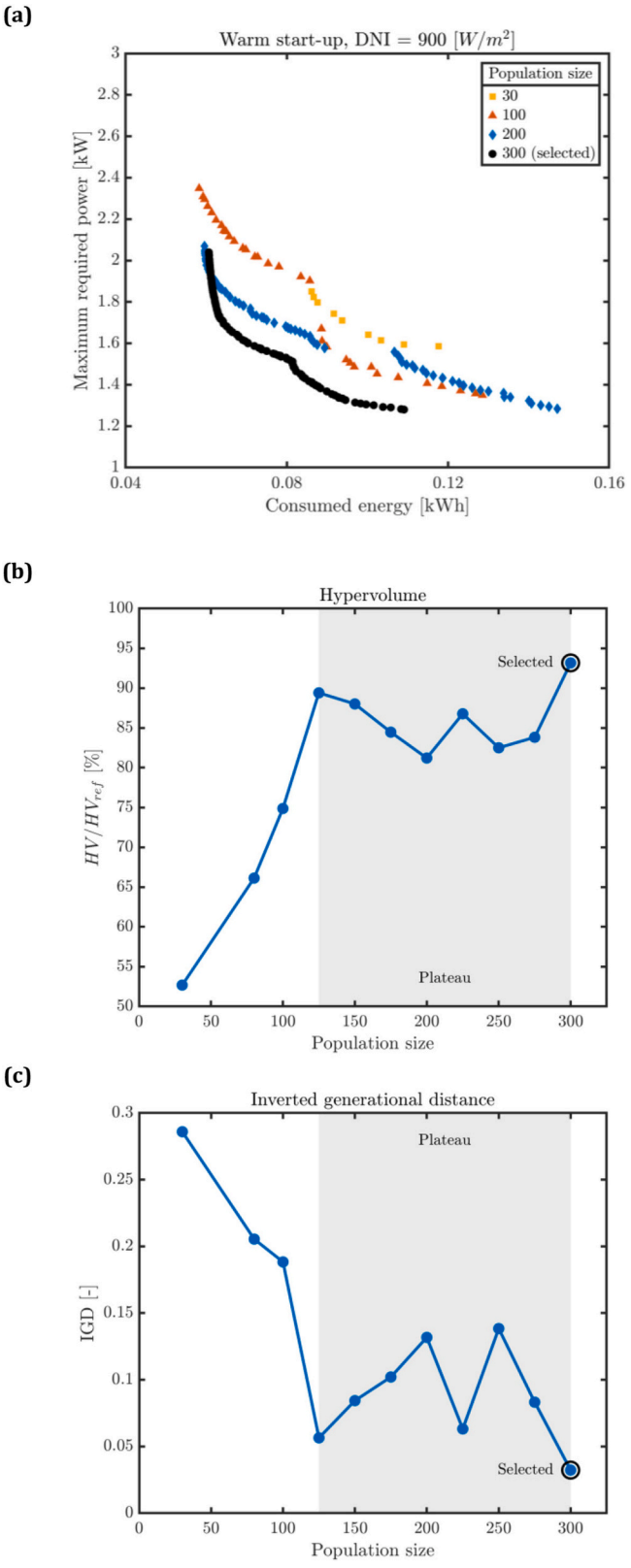


Fig. A1. Sensitivity of the Pareto front to the GA population size for the warm start-up at DNI = 900 W/m^2: (a) Pareto fronts for selected population sizes, (b) normalised hypervolume, (c) inverted generational distance.

Data availability

Data will be made available on request.

References

[1] G. Gavagnin, D. Sánchez, G.S. Martínez, J.M. Rodríguez, A. Muñoz, Cost analysis of solar thermal power generators based on parabolic dish and micro gas turbine: manufacturing, transportation and installation, Appl. Energy 194 (2017) 108–122, https://doi.org/10.1016/J.APENERGY.2017.02.052.

[2] M. Ghavami, J. Al-Zaili, A.I. Sayma, A methodology for techno-economic and operation strategy optimisation of micro gas turbine-based solar powered dish-engine systems, Energy 251 (2022) 123873, https://doi.org/10.1016/j.energy.2022.123873.

[3] Z. Ding, H. Hou, L. Duan, E. Hu, N. Zhang, J. Song, Performance analysis and capacity optimization of a solar aided coal-fired combined heat and power system, Energy 239 (2022) 122141, https://doi.org/10.1016/j.energy.2021.122141.

[4] Y.-L. He, et al., Perspective of concentrating solar power, Energy 198 (2020) 117373, https://doi.org/10.1016/j.energy.2020.117373.

[5] M. Boujoudar, et al., AI fault detection in CSP with simulation based fault injection on a 1 MWe Fresnel–ORC plant, Sol. Energy 303 (October 2025) (2026) 114089, https://doi.org/10.1016/J.SOLENER.2025.114089.

[6] A. Peinado Gonzalo, A. Pliego Marugán, F.P. García Márquez, A review of the application performances of concentrated solar power systems, Appl. Energy 255 (2019) 113893, https://doi.org/10.1016/j.apenergy.2019.113893.

[7] A.H. Samitha Weerakoon, M. Assadi, Trends and advances in micro gas turbine technology for sustainable energy solutions: a detailed review, Energy Convers. Manage.: X 20 (2023) 100483, https://doi.org/10.1016/J.ECMX.2023.100483.

[8] A. Kasaeian, E. Bellos, A. Shamaeizadeh, C. Tzivanidis, Solar-driven polygeneration systems: recent progress and outlook, Appl. Energy 264 (2020) 114764, https://doi.org/10.1016/j.apenergy.2020.114764.

[9] CORDIS EU research results (European Commission), SOLHYCO solar-hybrid power and cogeneration plants, Publications Office, 2011. https://cordis.europa.eu/project/id/19830/reporting.

[10] Directorate-General for Research and Innovation (European Commission), solar hybrid gas turbine electric power system, Publications Office, 2005. https://publications.europa.eu/en/publication-detail/-/publication/e4f88dd1-74ac-4416-aba0-3868cc8ea5ca/language-en.

[11] R. Korzynietz, et al., Solugas – comprehensive analysis of the solar hybrid Brayton plant, Sol. Energy 135 (2016) 578–589, https://doi.org/10.1016/j.solener.2016.06.020.

[12] J. Sinai, C. Sugarmen, U. Fisher, Adaptation and Modification of Gas Turbines for Solar Energy Applications, Proc. ASME Turbo Expo 5 (2008) 87–94, https://doi.org/10.1115/GT2005-68122.

[13] J. Yang, et al., Thermodynamic modelling and real-time control strategies of solar micro gas turbine system with thermochemical energy storage, J. Clean. Prod. 304 (2021) 127010, https://doi.org/10.1016/j.jclepro.2021.127010.

[14] F. Rovense, M. Amelio, N.M. Scornaienchi, V. Ferraro, Performance analysis of a solar-only gas micro turbine, with mass flow control, Energy Procedia 126 (2017) 675–682, https://doi.org/10.1016/J.EGYPRO.2017.08.296.

[15] M. Amelio, M.S. Pèrez, V. Ferraro, F. Rovense, S. Bova, Dynamic simulation of the temperature inlet turbine control system for an unfired micro gas turbine in a concentrating solar tower, Energy Procedia 148 (2018) 712–719, https://doi.org/10.1016/J.EGYPRO.2018.08.161.

[16] S. Zhang, M. Liu, Y. Zhao, J. Liu, J. Yan, Energy and exergy analyses of a parabolic trough concentrated solar power plant using molten salt during the start-up process, Energy 254 (2022) 124480, https://doi.org/10.1016/J.ENERGY.2022.124480.

[17] M.A. Khader, M. Ghavami, J. Al-Zaili, A.I. Sayma, Heat transfer effect on micro gas turbine performance for solar power applications, Energies (2021), https://doi.org/10.3390/en14206745.

[18] CORDIS EU research results (European Commission), final report summary - OMSoP optimised microturbine solar power system, Publications Office, 2017. https://cordis.europa.eu/project/id/308952/reporting.

[19] M. Lanchi, et al., Investigation into the coupling of micro gas turbines with CSP technology: OMSoP project, Energy Procedia 69 (0) (2015) 1317–1326, https://doi.org/10.1016/j.egypro.2015.03.146.

[20] B. Ssebabi, F. Dinter, J. van der Spuy, M. Schatz, Predicting the performance of a micro gas turbine under solar-hybrid operation, Energy 177 (2019) 121–135, https://doi.org/10.1016/j.energy.2019.04.064.

[21] I. Rossi, A. Sorce, A. Traverso, Gas turbine combined cycle start-up and stress evaluation: a simplified dynamic approach, Appl. Energy 190 (2017) 880–890, https://doi.org/10.1016/J.APENERGY.2016.12.141.

[22] F. Alobaid, R. Postler, J. Ströhle, B. Epple, H.G. Kim, Modeling and investigation start-up procedures of a combined cycle power plant, Appl. Energy 85 (12) (2008) 1173–1189, https://doi.org/10.1016/J.APENERGY.2008.03.003.

[23] A. Tică, Design, Optimization and Validation of Start-up Sequences of Energy Production Systems, 2012.

[24] I. Bertini, M. De Felice, F. Moretti, and S. Pizzuti, Start-Up Optimisation of a Combined Cycle Power Plant with Multiobjective Evolutionary Algorithms, in: Lecture Notes in Computer Science (including subseries Lecture Notes in Artificial Intelligence and Lecture Notes in Bioinformatics) 6025, LNCS, 2010, pp. 151–160, https://doi.org/10.1007/978-3-642-12242-2_16. PART 2.

[25] M. Quero, R. Korzynietz, M. Ebert, A.A. Jiménez, A. Del Río, J.A. Brioso, Solugas - operation experience of the first solar hybrid gas turbine system at MW scale, Energy Procedia 49 (2014) 1820–1830, https://doi.org/10.1016/j.egypro.2014.03.193.

[26] J.M. Llamas, D. Bullejos, M.R. De Adana, Optimal operation strategies into deregulated markets for 50 MWe parabolic trough solar thermal power plants with thermal storage, Energies 12 (5) (2019) 935, https://doi.org/10.3390/EN12050935.

[27] A. Traverso, S. Barberis, D. Lima, A.F. Massardo, Dynamic analysis of concentrated solar hybridised gas turbine 3A, Proceedings of the ASME Turbo Expo, 2014, https://doi.org/10.1115/GT2014-25225.

[28] J. Chen, G. Xiao, M.L. Ferrari, T. Yang, M. Ni, K. Cen, Dynamic simulation of a solar-hybrid microturbine system with experimental validation of main parts, Renew. Energy 154 (2020) 187–200, https://doi.org/10.1016/j.renene.2019.11.022.

[29] M. Lanchi, J. Al-Zaili, V. Russo, M. Falchetta, M. Montecchi, L. Aichmayer, A quasi-steady state model of a solar parabolic dish micro gas turbine demonstration plant, Energies (2022), https://doi.org/10.3390/en15031059.

[30] S.V. Hosseini, Y. Chen, S.H. Madani, M. Chizari, Annual performance evaluation of a hybrid concentrated solar–micro gas turbine based on off-design simulation, Heliyon 10 (10) (2024) e30717, https://doi.org/10.1016/J.HELIYON.2024.E30717.

[31] M. Ghavami, J. Alzaili, A.I. Sayma, A comparative study of the control strategies for pure concentrated solar power micro gas turbines. Proceedings of the ASME Turbo Expo 3, 2017, pp. 1–10, https://doi.org/10.1115/GT2017-63987.

[32] S. Shamekhi Amiri, J. Al-Zaili, A.I. Sayma, Development and validation of a transient electro-thermo- mechanical model for parabolic dish micro gas turbines, Energies 19 (5) (2026) 1188, https://doi.org/10.3390/EN19051188.

[33] P.P. Walsh, P. Fletcher, Gas Turbine Performance, 2nd edition, 2004.

[34] J. Kurzke, Gasturb 12 Design and off-Design Performance of Gas Turbines, Gasturb, Germany, 2012. https://www.gasturb.com/.

[35] W. Wang, H. Xu, B. Laumert, T. Strand, An inverse design method for a cavity receiver used in solar dish Brayton system, Sol. Energy 110 (2014) 745–755, https://doi.org/10.1016/J.SOLENER.2014.10.019.

[36] S.Y. Wu, F.H. Guo, L. Xiao, Numerical investigation on combined natural convection and radiation heat losses in one side open cylindrical cavity with constant heat flux, Int. J. Heat Mass Transf. 71 (2014) 573–584, https://doi.org/10.1016/J.IJHEATMASSTRANSFER.2013.12.064.

[37] H.M. Hofmann, M. Kind, H. Martin, Measurements on steady state heat transfer and flow structure and new correlations for heat and mass transfer in submerged impinging jets, Int. J. Heat Mass Transf. 50 (19–20) (2007) 3957–3965, https://doi.org/10.1016/J.IJHEATMASSTRANSFER.2007.01.023.

[38] F.P. Incropera, Fundamentals of Heat and Mass Transfer, John Wiley & Sons, Inc., Hoboken, NJ, USA, 2006.

[39] D. Iaria, H. Nipkey, J. Al Zaili, A.I. Sayma, M. Assadi, Development and validation of a thermo-economic model for design optimisation and off-design performance evaluation of a pure solar microturbine, Energies 11 (11) (2018) 3199, https://doi.org/10.3390/EN11113199.

[40] R.M. Manglik, A.E. Bergles, Heat transfer and pressure drop correlations for the rectangular offset strip fin compact heat exchanger, Exp. Thermal Fluid Sci. 10 (2) (1995) 171–180, https://doi.org/10.1016/0894-1777(94)00096-Q.

[41] S. Shamekhi Amiri, "Transient Analysis and Optimisation of Solar-Powered micro Gas Turbine Operation during Start-Up," PhD thesis, City University of London, 2023.

[42] P.K. Zachos, I. Aslanidou, V. Pachidis, R. Singh, A sub-idle compressor characteristic generation method with enhanced physical background, J. Eng. Gas Turbines Power 133 (8) (2011), https://doi.org/10.1115/1.4002820/408054.

[43] N.A. Cumpsty, Compressor aerodynamics, Longman Scientific & Technical, 1989, p. 509. Accessed: Oct. 07, 2025. [Online]. Available, http://www.amazon.com/Compressor-Aerodynamics-N-Cumpsty/dp/1575242478/ref=pd_sim_b_2%5Cnhttps://books.google.co.in/books/about/Compressor_aerodynamics.html?id=LNdSAAAAMAAJ&pgis=1.

[44] K. Deb, A. Pratap, S. Agarwal, T. Meyarivan, A fast and elitist multiobjective genetic algorithm: NSGA-II, IEEE Trans. Evol. Comput. 6 (2) (2002) 182–197, https://doi.org/10.1109/4235.996017.

[45] R. Electronics Corporation, IGBT IGBT Module Application Note, 2026.

[46] S. Maniktala, Component ratings, stresses, reliability, and life, Switching Power Supplies A - Z (2012) 241–280, https://doi.org/10.1016/B978-0-12-386533-5.00006-1.

[47] HOME - SoDa, Accessed: Dec. 14, 2025. [Online]. Available, https://www.soda-pro.com/home, 2026.

[48] C. Rigollier, M. Lefèvre, L. Wald, The method HELIOSAT-2 for deriving shortwave solar radiation from satellite images, Sol. Energy 77 (2004) 159–169.